

Enclosures

1. Yong Zhou, Shashikant A. Kadam, Mariya Shamzhy, Jiří Čejka, Maksym Opanasenko. Isoreticular UTL-derived zeolites as model materials for probing pore size-activity relationship. *ACS Catalysis*, 9(2019), 5136-5146.
doi.org/10.1021/acscatal.9b00950.
2. Yong Zhou, Naděžda Žilková, Mariya Shamzhy, Yamini Avadhut, Martin Hartmann, Jiří Čejka, Maksym Opanasenko. Novel approach towards Al-rich AFI for catalytic application. *Applied Catalysis A: General*, 577(2019), 62-68.
doi.org/10.1016/j.apcata.2019.03.015
3. Hua Chen, Yong Zhou, Zdeněk Tošner, Jiří Čejka, Maksym Opanasenko. Synthesis of aggregation-resistant MFI nanoparticles. *Catalysis Today*, (2019).
doi.org/10.1016/j.cattod.2019.10.026.

Declaration of Authorship

I declare that I have presented this thesis independently and I have properly cited all literatures. This work has not been submitted to obtain any other academic degree.

This work was based on the following publications:

1. Yong Zhou, Shashikant A. Kadam, Mariya Shamzhy, Jiří Čejka, Maksym Opanasenko. Isorecticular UTL-derived zeolites as model materials for probing pore size-activity relationship. *ACS Catalysis*, 2019, 9, 5136-5146.
2. Yong Zhou, Naděžda Žilková, Mariya Shamzhy, Yamini Avadhut, Martin Hartmann, Jiří Čejka, Maksym Opanasenko. Novel approach towards Al-rich AFI for catalytic application. *Applied Catalysis A: General*, 2019, 577, 62-68.
3. Hua Chen, Yong Zhou, Zdeněk Tošner, Jiří Čejka, Maksym Opanasenko. Synthesis of aggregation-resistant MFI nanoparticles. *Catalysis Today*, (2019). doi.org/10.1016/j.cattod.2019.10.026.

My contributions to these publications were as follows:

In the 1st paper, I optimized the synthesis conditions for isorecticular zeolite catalysts. I performed XRD characterization and tetrahydropyranylation reaction testing. I participated data analysis and wrote the initial manuscript. My overall contribution is 80 %.

In the 2nd paper, I optimized the alumination conditions for **AFI** germanosilicate zeolite, and performed XRD characterization. I participated data analysis and wrote the initial manuscript. The overall contribution is 70 %.

In the 3rd paper, I participated **MFI** nanosized zeolites preparation and DLS characterization and I performed acylation reaction testing. The overall contribution is 40 %.

Signature: *Yong Zhou*

Date: *27. 5. 2020.*


M. Opanasenko

Isorecticular UTL-Derived Zeolites as Model Materials for Probing Pore Size–Activity Relationship

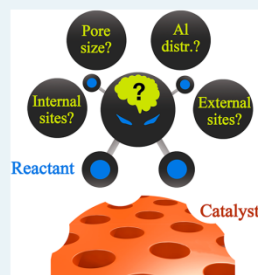
Yong Zhou, Shashikant A. Kadam,[✉] Mariya Shamzhy,^{*✉} Jiří Čejka, and Maksym Opanasenko^{*}

Department of Physical and Macromolecular Chemistry, Faculty of Science, Charles University in Prague, Hlavova 8, 128 43 Prague 2 Czech Republic

Supporting Information

ABSTRACT: The relationship between the chemical composition and the activity of zeolites has been unambiguously established and used to optimize some reactions. However, the relationship between the micropore size and the activity of catalysts remains elusive. Here, we report the combination of the ADOR approach and postsynthetic alumination for the preparation of isorecticular Al–IPC materials as model catalysts to assess the effect of micropore size on their catalytic activity. XRD, SEM, N₂ ad-/desorption, chemical analysis, ²⁷Al NMR, and FTIR spectroscopy of adsorbed acetonitrile-*d*₃ show that the prepared isorecticular Al–IPC zeolites have similar Al content and coordination states as well as similar types and total numbers of acid sites but differ in micropore size, decreasing in the following order: Al–IPC-7 (14, 12, and 10-ring channels) > Al–IPC-2 (12 and 10) > Al–IPC-6 (12, 10, and 8) > Al–IPC-4 (10 and 8). Furthermore, the kinetic study of gas-phase ethanol-to-diethyl ether transformation evidenced a lack of confinement in ethanol dimers of IPC-6 and IPC-4 ($k_{\text{first}} = 0.4\text{--}0.9 \text{ mol}_{\text{DEE}} (\text{mol}_{\text{H}^+}\cdot\text{s})^{-1}$) compared with IPC-2 ($k_{\text{first}} = 3.8 \text{ mol}_{\text{DEE}} (\text{mol}_{\text{H}^+}\cdot\text{s})^{-1}$) and IPC-7 ($k_{\text{first}} = 6.3 \text{ mol}_{\text{DEE}} (\text{mol}_{\text{H}^+}\cdot\text{s})^{-1}$) zeolites. The catalytic activity of IPC-zeolites in liquid-phase tetrahydropyranlation was correlated with the relative concentration of acid sites on the external surface of Al–IPC-*n* crystals, both increasing in the following order: IPC-4 (35% of “external” acid sites) < IPC-6 (29%) < IPC-2 (25%) < IPC-7 (21%). The use of Al–IPC-*n* as model catalysts in important acid-catalyzed reactions can shed a light on the fundamental structure–activity relationship and help to improve or optimize existing catalytic processes.

KEYWORDS: UTL zeolite, ADOR, acid sites, ethanol dehydration, tetrahydropyranlation



1. INTRODUCTION

Zeolites are a class of porous materials traditionally applied in industrial processes, such as fluid catalytic cracking,^{1,2} hydrocracking³ and alkylation.⁴ Recently emerging applications of zeolites have been extended to the production of fine chemicals.^{5,6} The performance of zeolite catalysts (activity, selectivity) largely depends on both pore size/connectivity (e.g., 8-, 10-, and 12-rings or even larger pore openings and one-, two-, or three-dimensional channel systems) and framework composition (e.g., Si/Al ratios).^{7–10} The relationship between the chemical composition and the activity of zeolites has been unambiguously established and used to optimize some processes, such as dehydrogenation,^{7,8} esterification,⁹ and methanol to olefin (MTO) reactions.¹⁰ In contrast, the effect of the distribution of active centers among pores of different sizes (which plays a role, e.g., in the stabilization of particular intermediates and products) on the catalytic performance of zeolites has been difficult to establish because variations in zeolite pore structure are necessarily accompanied by changes in zeolite topology. On the other hand, the comparison of the catalytic activity of zeolites with the same structure and chemical composition but with different micropore sizes enables a fair analysis of the role of micropore size in a specific reaction.

The recently developed unconventional zeolite synthesis method, ADOR (assembly disassembly organization–reassem-

bly),^{11–13} is an appropriate method for designing zeolites with predefined structure and porosity.^{14–19} In particular, the ADOR transformation of UTL germanosilicate is a facile route to produce a set of isorecticular IPC zeolites^{17–20} (Table 1), i.e., zeolites with the same crystalline layers but with different interlayer connectivity, represented by simple building units, as shown in Figure 1.

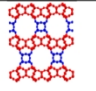
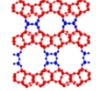
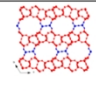
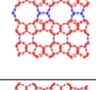
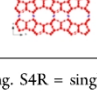
The UTL framework can be regarded as silicon-rich layers connected by germanium-rich, double-four-ring units (D4R).^{21,22} The outcome of the UTL transformation via the ADOR process strongly depends on the acidity of the reaction medium because two competing processes are involved: rearrangement and deintercalation.^{12,18} High acidity favors the rearrangement of silica at the interlayer sites, thus leading to the IPC-2 zeolite with single four-ring (S4R) interlayer connections.^{17,23} Complete removal of species from the interlayer space, facilitated under neutral or mild acidic conditions, results in the formation of the IPC-4 zeolite with only oxygen bridges between layers.¹⁷ When optimized conditions were applied, other new zeolites combining D4Rs, S4Rs, and oxygen bridges could be produced (Table 1). The IPC-7 zeolite containing both

Received: March 5, 2019

Revised: April 24, 2019

Published: April 26, 2019

Table 1. Structure of UTL and IPC-*n* Zeolites^a

Zeolite		Interlayer connection	Channel size, Å					
			14- ring	12- ring	12- ring	10- ring	10- ring	8- ring
UTL		D4R	9.5× 7.1	8.5× 5.5				
IPC-7		D4R, S4R	9.5× 7.1	8.5× 5.5	6.6× 6.2	5.4× 5.3		
IPC-2		S4R			6.6× 6.2	5.4× 5.3		
IPC-6		S4R, oxygen			6.6× 6.2	5.4× 5.3	5.8× 3.8	4.5× 3.6
IPC-4		oxygen					5.8× 3.8	4.5× 3.6

^aD4R = double four-ring. S4R = single four-ring.

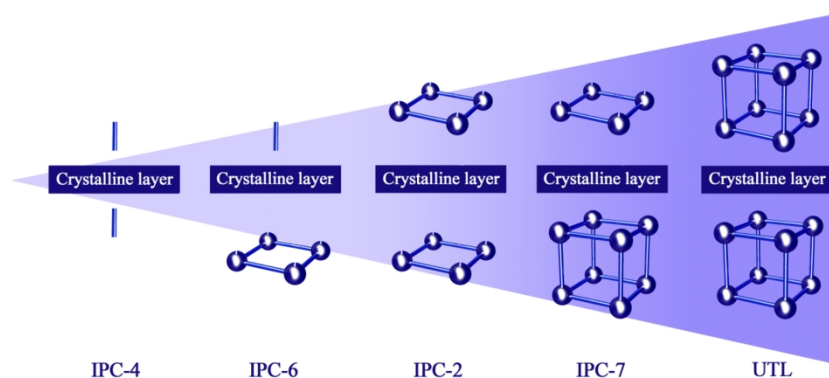


Figure 1. Examples of the alternating units that connect layers of the same structure in isorecticular zeolites. Spheres depict T atoms (Si, Al, Ge), whereas lines depict oxygen bridges.

D4Rs and S4Rs in a 1:1 ratio can be synthesized in acidic solutions at approximately $[H^+] = 3$ M, whereas the IPC-6 zeolite containing both S4Rs and oxygen bridges units can be synthesized at approximately $[H^+] = 1.5$ M.¹⁸

A comprehensive study of UTL and IPC-*n* zeolites by X-ray powder diffraction, transmission electron microscopy, Ar physisorption, and annihilation lifetime spectroscopy²⁴ showed the isorecticular character of the IPC-*n* family. The structure and

composition identity of IPC-*n* zeolites with various micropore sizes enabled us to assess the effect of micropore structure on carbon dioxide adsorption.²⁵ This family of isorecticular zeolites with tunable porosity may also be used to address the effect of micropore size on the catalytic performance.^{26,27}

Žilková et al.²⁸ have attempted to address the effect of UTL layer connectivity in isorecticular zeolites on their catalytic performance in toluene alkylation. However, significant differ-

ences in Al content ($\text{Si}/\text{Al} = 13\text{--}109$) with a large fraction of extra-framework Al atoms in IPC-*n* catalysts prevented them from reaching clear conclusions on the micropore structure–activity relationship. Therefore, the synthesis of isorecticular IPC catalysts with Al atoms predominantly located at framework positions and with similar Al content and acidity remains a considerable challenge.

Conversely, the specific location of the acid sites is known to affect the catalytic activity and selectivity of Al-containing zeolites.^{29–32} Since the structure of IPC zeolites prepared under different conditions varies, the location of acid sites within individual zeolites could also vary. Matsunaga et al.^{33,34} studied the location of Brønsted and Lewis acid sites in several MCM-22-type zeolites using IR methods with N_2 , CO, hexamethylenimine, or pivalonitrile as probe molecules and found that the reactivity of MWW catalysts in the MPV reduction of different ketones depends on the location of active Lewis acid sites. Wang et al.^{35–37} revealed that Al atoms preferably occupy intersectional T sites in H-ZSM-5. In contrast, these atoms are mainly located in the straight 10-ring channel of H-ZSM-11, as shown by several spectroscopy methods, *p*-xylene isomerization, and DFT calculations. These results clearly show that Al siting or the distribution of acid sites strongly affects the catalytic performance in MTO. Therefore, the effects of the location of acid sites and of the types of Al species in frameworks with different pore systems on the catalytic activity of the respective zeolites must be assessed to improve or optimize the corresponding catalytic processes.

In this work, we report the combination between the ADOR approach and postsynthetic alumination for the preparation of isorecticular Al–IPC zeolites without extra-framework Al and with a similar concentration of acid sites in micropores of different sizes. The structural and textural properties of the materials were characterized using XRD, N_2 ad-/desorption, SEM, and ^{27}Al NMR. The distribution of acid sites among the pores in Al–IPC was thoroughly characterized by FTIR spectroscopy of adsorbed probe molecules with different sizes (acetonitrile-*d*₃, quinoline) and by ethanol-to-diethyl ether kinetic analysis. Lastly, the catalytic behavior of aluminosilicate isorecticular zeolites in a liquid-phase batch-type reaction (tetrahydropyranlation with alcohols) was tested and discussed on the basis of their pore structure and on the location of acid sites.

2. EXPERIMENTAL SECTION

2.1. Zeolite Synthesis. **2.1.1. Synthesis of UTL Zeolites.** Germanosilicate UTL zeolite was synthesized using (6*R*,10*S*)-6,10-dimethyl-5-azoniaspiro[4,5]decane hydroxide as the structure-directing agent (SDA).³⁸ The molar composition of the reaction mixture was $0.6\text{--}0.8\text{SiO}_2/0.4\text{--}0.6\text{GeO}_2/0.4\text{SDA}/30\text{H}_2\text{O}$. Aluminum-containing UTL (Al–UTL) was synthesized using 7-ethyl-6-azoniaspiro[5.5]undecane hydroxide as SDA³⁹ from the reaction gel with a molar ratio of $0.788\text{SiO}_2/0.4\text{GeO}_2/0.012\text{AlO}_{1.5}/0.4\text{SDA}/30\text{H}_2\text{O}$. Typically, germanosilicate UTL was prepared by dissolving germanium dioxide (Sigma-Aldrich, 99.99%) in the aqueous solution of SDA. After 30 min, silica (Cab-O-Sil M5, Supelco Analytical) was added to the solution, and the mixture was stirred at room temperature. Subsequently, the resulting fluid gel was charged into 25 mL Teflon-lined stainless-steel autoclaves and heated to 175 °C for 7 days under agitation. The as-synthesized solid product was recovered by filtration, washed with distilled water, and dried overnight at 65 °C. For the Al-containing UTL sample, $\text{Al}(\text{OH})_3$

(Sigma-Aldrich) was dissolved first in the aqueous solution of SDA and then in germanium dioxide, subsequently adding silica. Finally, the above mixture remained under vigorous stirring to adjust the pH of the gel to 12 according to ref 39. The resulting fluid gel was charged into 25 mL of Teflon-lined stainless-steel autoclaves and heated to 175 °C for 22 days under agitation. To remove the SDA, the as-synthesized zeolites were calcined in air at 550 °C, 1 °C/min for 6 h. The calcined samples were used as the starting material of postsynthetic alumination to synthesize Al–IPC zeolites according to the following procedures.

2.1.2. Synthesis of Al–IPC-*n* Isorecticular Zeolites. **Al–IPC-7:** 1 g of calcined Al–UTL zeolite was mixed with 100 mL of a 3 M aqueous $\text{Al}(\text{NO}_3)_3$ solution at 60 °C for 16 h. After alumination, the solid was isolated by centrifugation, washed with 0.01 M HCl and water, dried at 65 °C overnight, and calcined at 550 °C for 6 h.

Al–IPC-2: 1 g of calcined Al–UTL zeolite was mixed with 100 mL of 1 M aqueous $\text{Al}(\text{NO}_3)_3$ solution at room temperature for 16 h. After alumination, the solid was isolated by centrifugation, washed with 0.01 M HCl and water, dried at 65 °C overnight, and calcined at 550 °C for 6 h.

Al–IPC-6: 1 g of calcined UTL zeolite ($\text{Si}/\text{Ge} = 2$ in gel) was stirred in a mixture of 150 mL of 1 M acetic acid and 100 mL of 1 M $\text{Al}(\text{NO}_3)_3$ solutions at 95 °C for 16 h. The solid was isolated by centrifugation, washed with 0.01 M HCl and water, dried at 65 °C overnight, and treated with octylamine (solid-to-liquid ratio = 1:50 w/w) at 60 °C for 16 h. The final product was calcined at 550 °C for 6 h.

Al–IPC-4: 1 g of calcined UTL zeolite ($\text{Si}/\text{Ge} = 1$ in gel) was stirred in a mixture of 150 mL of 1 M acetic acid and 100 mL of 1 M $\text{Al}(\text{NO}_3)_3$ solutions at 95 °C for approximately 16 h. The solid was isolated by centrifugation, thoroughly washed with 0.01 M HCl and water, dried, and then treated with octylamine (solid-to-liquid ratio = 1:50 w/w) at 60 °C for 16 h. The final product was calcined at 550 °C for 6 h.

2.2. Characterization of the Catalysts. The structure and phase purity of the catalysts were validated using X-ray powder diffraction (XRD). The XRD patterns were measured with a Bruker AXS-D8 Advance diffractometer equipped with a graphite monochromator and a position sensitive detector (Vantec-1) at a scan rate of 0.25° (2θ per minute) using Cu $K\alpha$ radiation. The chemical composition of zeolites was analyzed by ThermoScientific iCAP 7000 ICP/OES. The crystal morphology was assessed by scanning electron microscopy (SEM) using a JEOL JSM-5500 LV microscope. An ASAP 2020 (Micromeritics) static volumetric apparatus was used to measure N_2 ad-/desorption isotherms at $T = -196$ °C (liquid nitrogen temperature). Prior to the N_2 adsorption, zeolites were activated at $T = 250$ °C for 4 h while being degassed with a turbomolecular pump. The concentrations of Lewis (c_L) and Brønsted (c_B) acid sites were evaluated using FTIR spectroscopy of adsorbed acetonitrile-*d*₃ (ACN). The zeolites were pressed into self-supporting wafers with a density of $8\text{--}10\text{ mg}\cdot\text{cm}^{-2}$ and activated in situ at $T = 450$ °C and at $P < 1 \times 10^{-4}$ Torr for 4 h. This was followed by desorption at the same temperature for 30 min. The spectra were recorded with a resolution of 4 cm^{-1} using a Nicolet 6700 FT-IR spectrometer equipped with a transmission MCT/B detector. ACN adsorption was performed at $T = 25$ °C and at a partial pressure $p_{\text{AN}} = 3.0$ Torr for 30 min. c_B and c_L were evaluated based on the intensity of the bands at 2300 cm^{-1} ($\mathcal{E}(\text{B}) = 2.05 \pm 0.1\text{ cm}\cdot\mu\text{mol}^{-140}$) and 2330 cm^{-1} ($\mathcal{E}(\text{L}) = 3.6 \pm 0.2\text{ cm}\cdot\mu\text{mol}^{-140}$), respectively.

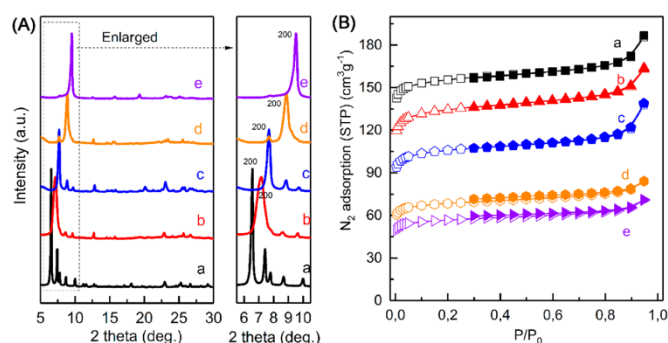


Figure 2. (A) XRD patterns; (B) N_2 adsorption and desorption isotherms of the parent Al–UTL and isorecticular Al-containing IPC-7 (b), IPC-2 (c), IPC-6 (d), and IPC-4 (e) zeolite catalysts.

Table 2. Physicochemical Properties of the Parent UTL and Al–IPC Samples

material	Si/Al ^d ratio	V_{tot} (cm ³ g ⁻¹)	V_{micro} ^b (cm ³ g ⁻¹)	S_{BET} ^c (m ² g ⁻¹)	$c_{Bronsted}$ ^d (mmol g ⁻¹)	c_{Lewis} ^d (mmol g ⁻¹)	c_{acid} (mmol g ⁻¹)
UTL		0.301	0.213	580			
Al–UTL	64.6	0.289	0.231	566	0.04	0.06	0.10
Al–IPC-7	20.1	0.263	0.194	485	0.15	0.24	0.39
Al–IPC-2	26.2	0.191	0.128	325	0.17	0.20	0.37
Al–IPC-6	24.9	0.130	0.099	249	0.14	0.23	0.37
Al–IPC-4	20.5	0.110	0.082	207	0.19	0.21	0.40

^aMeasured by ICP. ^bCalculated using the t-plot method. ^cSpecific surface area (BET) given by N_2 adsorption at -196 °C. ^dMeasured by FTIR after ACN adsorption.

“Internal” acid sites were discriminated from those located in extra-large pores and on the external surface (“external” acid centers) of Al–IPC-*n* zeolites by coadsorption of bulky quinoline and ACN. Quinoline adsorption was performed according to refs 41 and 42. Subsequently, the amount of “internal” acid centers being inaccessible for quinoline was probed by AN, as described above.

An Agilent DD2 500WB spectrometer was used for collecting ²⁷Al MAS NMR spectra at a resonance frequency of 130.24 MHz using a sample spinning rate of 15 kHz.

2.3. Catalytic Tests. **2.3.1. Tetrahydropyranylation of Alcohols.** The liquid-phase tetrahydropyranylation reaction was performed under atmospheric pressure at 60 °C in a multiexperiment workstation Star-Fish (Radleys Discovery Technologies). Before the catalytic test, 50 mg of the zeolite was activated for 90 min at $T = 450$ °C. Typically, alcohol (4.5 mmol), internal standard (0.25 g of mesitylene), and the catalyst were added to a two-necked flask equipped with a thermometer. 3,4-Dihydro-2H-pyran (DHP, 10 mL) was added to the flask when the required temperature was reached. Probes of the reaction mixture were taken periodically and analyzed using a gas chromatograph (Agilent 6859) equipped with a DB-WAX column (20 m × 0.18 mm × 0.3 μm) and with an FID detector.

2.3.2. Ethanol Dehydration. Steady-state gas-phase ethanol dehydration reaction over Al–IPC zeolites was performed at 185 °C under atmospheric pressure while varying partial pressures of ethanol nonmonotonically. First, the catalyst was activated under an oxygen flow (30 cm³/min) at 450 °C for 5 h. Ethanol partial pressure was adjusted by changing (i) the temperature in the saturator (7 and 30 °C for lower and higher ethanol partial pressure, respectively) and (ii) the degree of ethanol dilution with N_2 .

The products were analyzed on an online Agilent 6850 GC equipped with a DB-5 column (50 m × 0.32 mm × 1 μm) and with an FID detector. Ethanol conversion did not exceed 10%, and catalyst deactivation was not observed under used experimental conditions.

3. RESULTS AND DISCUSSION

3.1. Physicochemical Properties of Zeolites. By combining the ADOR approach with postsynthetic alumination, four Al-containing isorecticular IPC zeolites (IPC-7, IPC-2, IPC-6, and IPC-4) were synthesized using Al–UTL (for IPC-7 and IPC-2) or germanosilicate UTL (for IPC-6 and IPC-4) as starting materials.

3.1.1. Structure and Textural Properties. The XRD patterns of all synthesized Al–IPC-*n* zeolites (Figure 2A) matched those of silica analogues reported in the literature,^{17,18} thus showing the phase purity of all samples. Similar profiles (e.g., 12.7°, 15.7°, 22.9°, 25.2° 2θ) of the intralayer reflections observed in all samples confirmed the identity of their intralayer structure. Conversely, the shift of the interlayer peak (200) to 2θ higher values shows decreasing interlayer *d*-spacing in the following order of zeolites: UTL (6.1 2θ) > IPC-7 (6.9 2θ) > IPC-2 (7.8 2θ) > IPC-6 (8.5 2θ) > IPC-4 (9.7 2θ).

N_2 adsorption/desorption isotherms of Al–UTL and Al–IPC-*n* samples (Figure 2B) belong to type-I zeolites without a hysteresis loop, thus demonstrating purely microporous materials. Micropore volume decreases in the following order (Table 2): UTL (0.23 cm³ g⁻¹) > IPC-7 (0.19 cm³ g⁻¹) > IPC-2 (0.13 cm³ g⁻¹) > IPC-6 (0.10 cm³ g⁻¹) > IPC-4 (0.08 cm³ g⁻¹). This order matches the gradual decrease in interlayer spacing and hence in micropore size.

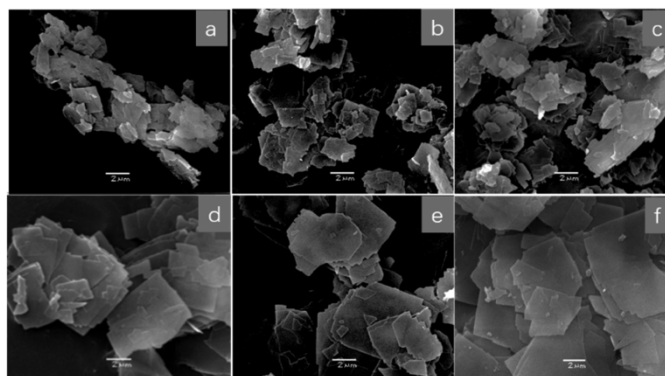


Figure 3. SEM of the parent Al-UTL (a), Ge-UTL (d), and isorecticular Al-containing IPC-7 (b), IPC-2 (c), IPC-6 (e), and IPC-4 (f) zeolite catalysts.

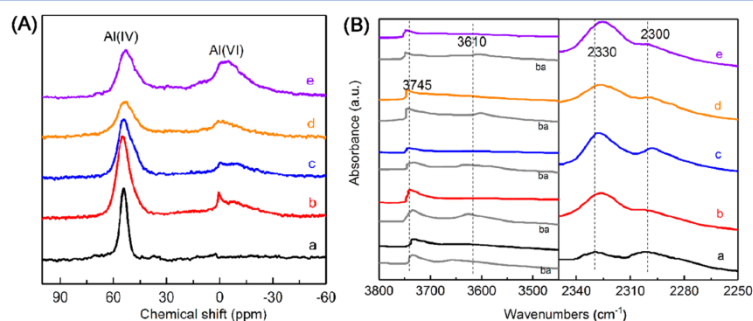


Figure 4. (A) ^{27}Al MAS NMR and (B) FTIR spectra of AN adsorbed in the parent Al-UTL (a) and isorecticular Al-containing IPC-7 (b), IPC-2 (c), IPC-6 (d), IPC-4 (e), and zeolite catalysts. Gray lines (ba) show the spectra of the respective samples after activation.

SEM images reveal that the crystals maintain their shape and size upon UTL-to-IPC transformation (Figure 3). Al-IPC-6 (Figure 3e) and Al-IPC-4 (Figure 3f) materials showed uniform platelike crystals (2–4 μm) similar to those of the parent UTL (Figure 3d) germanosilicate zeolite, whereas the crystal sizes of Al-IPC-2 (Figure 3c) and Al-IPC-7 (Figure 3b) samples were slightly smaller than that of the parent Al-UTL ($\sim 2 \mu\text{m}$, Figure 3a).

^{27}Al NMR spectra showing a dominating peak of tetrahedrally coordinated Al atoms at 55 ppm and a small reflex of octahedrally coordinated Al at 0 ppm clearly showing the incorporation of most Al atoms into the framework positions of IPC-*n* zeolites (Figure 4A). Importantly, the duration of zeolite treatment with 0.01 M HCl had no effect on the intensity of the peak at 55 ppm corresponding to tetrahedrally coordinated aluminum for all Al-IPC-*n* zeolites. Simultaneously, complete removal of octahedrally coordinated Al from the IPC-7 zeolite required prolonging the washing treatment to 25 min (Figure S1). In accordance with the chemical analysis, the Si/Al ratio of IPC-7 increased from 13 to 20.1 upon acid treatment.

Thus, the results clearly show that the concentration of extra-framework Al species in IPC samples can be changed by modulating the acid-washing period, thereby preparing a set of

isorecticular zeolites with similar Si/Al ratios of approximately 20 (Table 1).

3.1.2. Type and Concentration of Acid Sites. The type and total concentration of acid sites in Al-IPC-*n* samples are determined by FTIR of adsorbed ACN with a kinetic diameter (4.0 Å) small enough to access acid sites, even in 8-ring channels. As shown in Figure 4B, before ACN adsorption (“ba”), all samples show bands around 3745 and 3620 cm^{-1} assigned to silanol and acidic bridging OH groups ($\equiv\text{Si}(\text{OH})-\text{OH}-\text{Al}\equiv$), respectively. The adsorption of ACN removed the band around 3620 cm^{-1} , whereas new characteristic absorption bands appeared at 2300 and 2330 cm^{-1} , thus indicating that ACN molecules interact with Brønsted and Lewis acid sites, respectively.

All Al-IPC samples under investigation have similar concentrations of both Brønsted and Lewis acid sites (Table 2), exceeding 3–4 times the values characteristic of Al-UTL zeolites. The markedly lower number of acid sites in Al-UTL is caused by the narrow field of pure UTL phase crystallization in Al-containing reaction mixtures, as shown in ref 39.

Although we used ACN to probe the total concentration of acid sites in Al-IPC zeolites (Table 2 and Figure 4B), sequential adsorption of quinoline and ACN was applied to differentiate acid sites located in small (8-ring), medium (10-ring), and large

(12 ring) pore containing channel systems (“internal” acid sites) from those located in extra-large pores and on the external surface (“external” acid sites). A previous study has shown that quinoline can be adopted to determine acid sites located on the external surface and in extra-large pores of zeolites albeit without penetrating deep inside pores with a diameter smaller than 0.7 nm.⁴³ IR spectra of ACN adsorbed in activated Al–IPC-2, IPC-4, and IPC-6 and those collected after quinoline preadsorption are compared in Figure S2. In all samples, quinoline preadsorption unsurprisingly decreased the intensities of the peaks attributed to the interaction between ACN and Brønsted (2300 cm⁻¹) and Lewis (2315 and 2325 cm⁻¹) acid sites. Thus, the comparison between the total concentration of acid sites (Table 2) and the number of acid centers accessible for ACN after quinoline preadsorption allowed the selective determination of the Al siting of both noninterconnected pore systems of the IPC-7 zeolite and of pore systems located on the external surface and in the micropores of IPC-2, IPC-6, and IPC-4 zeolites (Figure 5B). The concentrations of Brønsted and Lewis

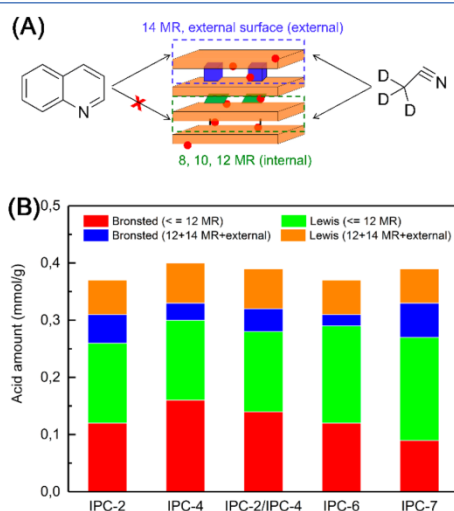


Figure 5. (A) Schematic description of quinoline and acetonitrile on Al–IPC zeolites and (B) distribution of acid sites of Al–IPC zeolites.

acid sites located on the external surface and in extra-large pores decrease with the increase in the crystal size of the catalysts, e.g., accounting for 35%, 29%, 25%, and 21% of the total number of acid sites of IPC-7, IPC-2, IPC-6, and IPC-4, respectively.

Thus, the chemical analysis, ²⁷Al NMR, and FTIR spectroscopy results showed the similarity between isorecticular Al–IPC zeolites with respect to the content and coordination state of Al and to the type and total number of acid sites, whereas the distribution of acid sites among micropores and the external surface of catalyst crystals slightly varies, thus reflecting differences in their size. Concomitantly, isorecticular IPC zeolites have micropores with markedly different sizes, ranging from the ones restricted with 8- to 14-ring channels, which is reflected in the decrease in the micropore volume in the following order: Al–IPC-7 > Al–IPC-2 > Al–IPC-6 > Al–IPC-4.

3.2. Catalytic Performance of Al–IPC Zeolites in Ethanol Dehydration.

To shed light on the siting of acid sites in micropores of different sizes, we further analyzed the performance of Al–IPC catalysts in the Brønsted acid-catalyzed ethanol dehydration reaction known to occur through a unimolecular route to produce ethylene or through a bimolecular pathway to generate diethyl ether (DEE). The choice of this reaction also allows us to experimentally validate the confinement effect on reaction rates by studying structure–activity relationships in the Al–IPC zeolite family.^{44–46} Figure 6 shows the turnover rates of DEE (R_{DEE}) and ethylene (R_{ethylene}) formation as a function of ethanol partial pressure at 185 °C. Figure 6 also shows that DEE is a major product in the whole range of ethanol partial pressures for all catalysts tested (Figure 6a). Ethylene production over IPC-7 and IPC-2 catalysts follows the well-established trend for a number of medium- and large-pore zeolites.^{44,45} The increase in R_{ethylene} with ethanol pressure at $0 < p_{\text{EtOH}} < 10$ mbar and the decrease in R_{ethylene} with the increase in p_{EtOH} at $p_{\text{EtOH}} > 10$ mbar was explained by the inhibition of ethylene synthesis via the formation of ethanol dimers at high pressures. Interestingly, R_{ethylene} remained stable in IPC-6 and IPC-4 when p_{EtOH} was increased to >0.01 bar, thus suggesting a limited formation of ethanol dimers in catalyst channels, even at high p_{EtOH} .

The analysis of the variation of ethanol-to-DEE dehydration turnover rates (R_{DEE}), normalized per total concentration of Brønsted sites determined from ACN adsorption) as a function of p_{EtOH} over Al–IPC zeolites (Figure 6A) shows a linear increase in R_{DEE} with p_{EtOH} (the first order kinetic) at low ethanol partial pressures (0.15–2.14 mbar) and an asymptotic, nonlinear R_{DEE} vs p_{EtOH} function (zero order kinetic) at higher ethanol pressures (2.14–102 mbar). Such function suggests that ethanol dehydration followed the associative dehydration pathway in all studied Al–IPC zeolites, yielding diethyl ether as a major product. The associative dehydration mechanism involves the adsorption of an ethanol molecule over the Brønsted acid site (ethanol monomer) followed by the adsorption of a second ethanol molecule over the same Brønsted acid site, thereby forming an ethanol dimer.⁴⁶ The activation of dimer results in the formation of transition state, which decomposes into water and adsorbed diethyl ether species. These species desorb, thus regenerating the Brønsted acid sites (Scheme 1). This sequence of elementary steps leads to following rate expression (the full derivation is shown in ref 47)

$$R_{\text{DEE},A} = \frac{k_{\text{first}} p_{\text{EtOH}}}{1 + \frac{k_{\text{first}}}{k_{\text{zero}}} p_{\text{EtOH}}} \quad (1)$$

where

$$k_{\text{first}} = k_{\text{DEE},A} K_p K_D \quad (2)$$

and

$$k_{\text{zero}} = k_{\text{DEE},A} K_p \quad (3)$$

where $K_{\text{DEE},A}$ is a rate constant and K_p and K_D are the adsorption equilibrium constants for coadsorbed state and dimer formation, respectively. k_{first} and k_{zero} are the apparent first-order and zero-order rate constants for the associative dehydration pathway.

The activation energy associated with the apparent first-order rate constants (k_{first}) reflects the energy difference between the transition state of the reaction of ether formation and the hydrogen-bonded ethanol monomer. Since the transition state and the ethanol monomer differ in charge distribution and size,

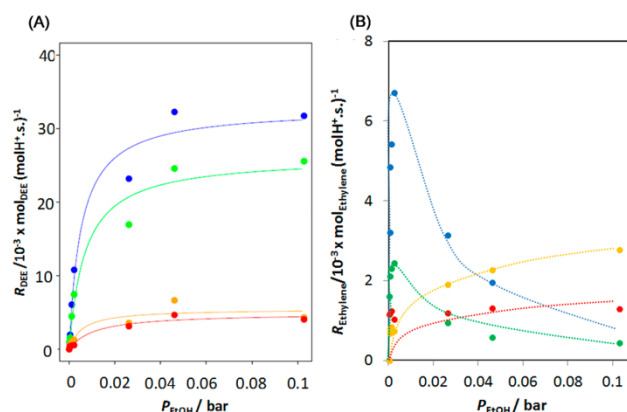
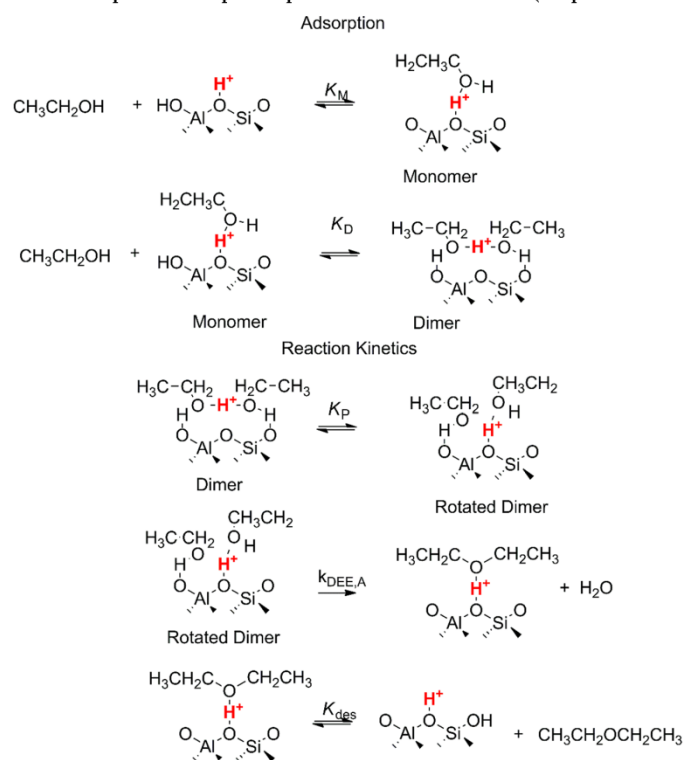


Figure 6. (A) Ethanol-to-DEE ($R_{\text{DEE}}/\text{mol}_{\text{DEE}} (\text{mol H}^+\cdot\text{s})^{-1}$) (data fitted to eq 1) and (B) ethanol-to-ethylene ($R_{\text{ethylene}}/\text{mol}_{\text{ethylene}} (\text{mol H}^+\cdot\text{s})^{-1}$) dehydration turnover rates (lines are the guide to the eye) over IPC-7 (blue), IPC-2 (green), IPC-6 (orange), and IPC-4 (red) at 185 °C.

Scheme 1. Schematic Representation of the Associative Ethanol Dehydration Pathway Showing Elementary Adsorption and Reaction Steps as Well as the Respective Adsorption Equilibrium and Rate Constants (Adapted from Kadam and Shamzhy⁴⁶)



k_{first} is sensitive to differences in both acid strength and porosity.^{48,49} Conversely, the activation energy associated with the apparent zero-order rate constants (k_{zero}) reflects the energy

of same transition state but relative to that of a protonated dimer. In contrast to k_{first} , k_{zero} remains similar among zeolites with different pore sizes because the protonated dimers and transition

state of the reaction of dimethyl ether formation are similar in size and thus in their van der Waals interactions with the zeolite wall.⁴⁹

The data shown in Figure 6A were fitted to eq 1, and the values of k_{first} and k_{zero} were extracted (Figure 7). The values of

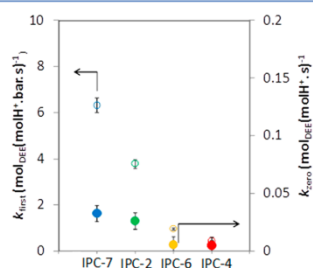


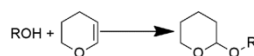
Figure 7. Rate constants k_{first} ($P_{\text{EtOH}} < 2.14$ mbar) and k_{zero} ($P_{\text{EtOH}} > 2.14$ mbar) of Al-IPC catalysts.

zero-order rate constants (close symbols, Figure 7) k_{zero} remain almost similar when comparing IPC-7 with IPC-2 and IPC-6 with IPC-4, but IPC-6 and IPC-4 have significantly lower constants than IPC-7 and IPC-2. Smaller k_{first} and k_{zero} clearly indicate space restrictions in the formation of ethanol dimers and in the corresponding transition state when comparing IPC-6 and IPC-4 vs IPC-7 and IPC-2. Figure 6B confirms this explanation, as shown by the variation in the turnover rate of ethylene formation (R_{ethylene}) as a function of p_{EtOH} . The turnover rates of ethylene formation over IPC-7 and IPC-2 gradually decrease with the increase in pressure due to the formation of ethanol dimers in the larger pores (14R and 12R) of the aforementioned zeolites.^{46–49} However, the R_{ethylene} of IPC-6 and IPC-4 remain constant, albeit slightly increasing at higher ethanol pressures. It confirms a limited dimer formation and the protection of ethoxide species, which are formed in the smaller pores (10R and 8R) of IPC-6 and IPC-4.⁴⁹ The higher value of k_{first} for Al-IPC-6 vs Al-IPC-4 is consistent with a better van der Waals stabilization of the transition state (rotated dimer in Scheme 1) than of H-bonded $\text{C}_2\text{H}_5\text{OH}$ molecule in 10×12 -ring channels of Al-IPC-6.⁴⁹ Higher concentration of acid sites in 10×12 -ring channels of IPC-2 vs IPC-6 naturally resulted in a further increase in the k_{first} value. In accordance with refs 45–49, the k_{first} value of IPC-7 is 1.5 times higher than that of IPC-2 at similar k_{zero} values for both catalysts, which may be explained by the higher concentration of Al atoms in the 10-ring channels of the IPC-7 zeolite.

Thus, the present data represent a predictive analysis of the structure–function relationship between Al siting and resulting kinetics. The present kinetic data contributes to developing methods for Al siting estimation in a given zeolite structure using the marked effects of active sites and surrounding confinement on kinetic rate constants, which are sensitive to such environments.

3.3. Catalytic Performance of Al-IPC Zeolites in Tetrahydropyranlation of Alcohols. **3.3.1. Al-IPC catalysts.** The effect of the distribution of acid sites among pores of different sizes on the catalytic behavior of Al-IPC zeolites was investigated in liquid-phase tetrahydropyranlation of alcohols with DHP, which is known to be catalyzed by both Brønsted and Lewis acid sites (Scheme 2).^{50,51}

Scheme 2. Tetrahydropyranlation of Alcohols



When a small ethanol molecule was used as reactant, all IPC catalysts showed similar activity, completely converting the substrate into the target product after 24 h (Figure 8). In

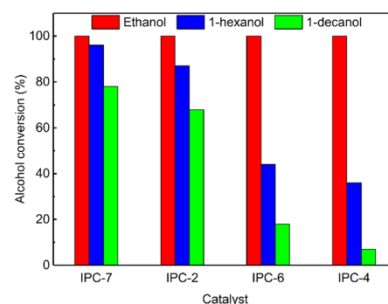


Figure 8. Alcohol conversion for the tetrahydropyranlation of ethanol, 1-hexanol, and 1-decanol after 24 h with DHP over Al-IPC catalysts under the following reaction conditions: 50 mg of catalyst, 4.5 mmol pf alcohol, 5 mL of DHP, and 0.25 g of mesitylene at 60 °C.

contrast, when using 1-hexanol, the IPC-4 catalyst reached only 36% conversion after 24 h, whereas the reactant conversion substantially increased when using IPC-7 as catalyst (over 90% conversion after 24 h, Figure 8). The four zeolites were also applied in the tetrahydropyranlation of 1-decanol, which provided further information on the effect of catalyst pore structure on its performance. Although lower conversion rates of 1-decanol vs 1-hexanol were assessed over all Al-IPC catalysts under investigation, IPC-7 was again the most active catalyst (78% conversion after 24 h). In general, the catalytic activity of zeolites in the tetrahydropyranlation of either 1-hexanol or 1-decanol correlates with the relative concentration of “external” acid sites, i.e., decreases with micropore size/volume in the following order: IPC-7 > IPC-2 > IPC-6 > IPC-4. These results suggest that, due to diffusion limitations, bulky reagents have limited access to the internal active sites of IPC zeolites and that IPC-4 has the lowest porosity has is the zeolite most affected by diffusion limitations.

3.3.2. Al-IPC-6 vs Al-IPC-2/IPC-4 catalyst. The average structure of the IPC-6 zeolite can be considered a combination of IPC-2 and IPC-4 (Figure S3). This makes it possible to compare materials with the same morphology, textural properties, and total concentration of acid sites but differing in structural organization, i.e., Al-IPC-6 (intergrown IPC-4 and IPC-2 frameworks) and the physical mixture of Al-IPC-4 and Al-IPC-2. We were able to prepare the physical mixture of IPC-2/IPC-4 catalysts (40% IPC-2 and 60% IPC-4), which has similar morphology to and the same porosity and number of acid sites as IPC-6 (Table S1). The distribution of acid sites in IPC-2/IPC-4 and in IPC-6 is different, as shown by acetonitrile-IR preadsorbed with quinoline. The composite catalyst IPC-2/IPC-4 has a higher concentration of external acid sites than the IPC-6 zeolite, 0.11 mmol/g (30%) and 0.08 mmol/g (25%), respectively (Figure 5).

We compared the behavior of the IPC-6 zeolite with that of the mechanical mixture of IPC-2/IPC-4 to further understand the effect of the distribution of acid sites on the catalytic performance of zeolites in the tetrahydropyranlation of different alcohols. IPC-6 and IPC-2/IPC-4 showed the same ethanol conversion rates, whereas the conversion rates of bulkier 1-hexanol and 1-decanol were significantly higher than those of IPC-2/IPC-4 (Figure 9). Considering the similar morphology,

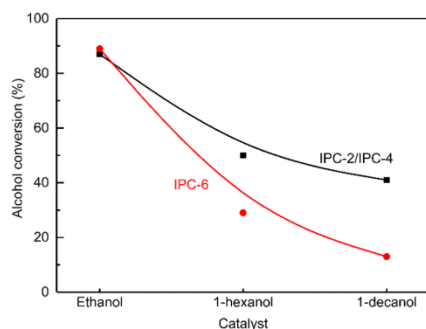


Figure 9. Conversion rates of the tetrahydropyranlation of ethanol, 1-hexanol, and 1-decanol with DHP over IPC-2/IPC-4 and IPC-6 catalysts at 6 h. Reaction conditions: 50 mg of catalyst, 4.5 mmol of alcohol, 5 mL of DHP, and 0.25 g of mesitylene at 60 °C.

porosity, and total concentration of acid sites of both catalysts, such a difference in their performance can be attributed to differences in the distribution of acid sites in IPC-6 vs IPC-2/IPC-4, i.e., to the lower concentration of “external” acid sites in IPC-6.

4. CONCLUSIONS

A set of isorecticular Al-IPC-*n* aluminosilicate zeolites with similar morphology, crystal size, Al content, and concentration of acid sites (0.37–0.40 mmol g⁻¹) but with different distributions of acid sites and gradually smaller channel sizes has been synthesized for the first time. FTIR spectroscopy of adsorbed probe molecules of variable size (*d*₃-acetonitrile, quinoline) revealed an increasing concentration of acid sites located on the external surface and in extra-large pores (“external” acid sites) in the following order: IPC-4 (21%) < IPC-6 (25%) < IPC-2 (29%) < IPC-7 (35%). Ethanol-to-diethyl ether kinetic study showed a lack of confinement of ethanol dimers in IPC-6 and IPC-4 ($k_{\text{first}} = 0.4\text{--}0.9 \text{ mol}_{\text{DEE}} (\text{mol}_{\text{H}_2\text{O}}\text{-s})^{-1}$) compared with IPC-2 ($k_{\text{first}} = 3.8 \text{ mol}_{\text{DEE}} (\text{mol}_{\text{H}_2\text{O}}\text{-s})^{-1}$) and especially with IPC-7 ($k_{\text{first}} = 6.3 \text{ mol}_{\text{DEE}} (\text{mol}_{\text{H}_2\text{O}}\text{-s})^{-1}$) zeolites. The better van der Waals stabilization of the transition state than that of H-bonded C₂H₅OH molecule in IPC-7 vs IPC-2 zeolite explains the higher concentration of Al atoms in 10-ring channels of the former catalyst. The comparison between the catalytic behavior of model catalysts (i.e., the IPC-6 zeolite and a mechanical mixture of IPC-2/IPC-4) with similar textural properties and total concentration of acid sites but with different distributions of acid centers allowed us to correlate catalyst activity in the tetrahydropyranlation of bulky 1-decanol with the number of “external” acid sites. Furthermore, while performing similarly in reactions with ethanol, the catalytic activity of IPC-*n* zeolites in the tetrahydropyranlation of bulky

1-decanol differed drastically and decreased with the concentration of “external” acid sites: IPC-7 > IPC-2 > IPC-6 > IPC-4. IPC-6 has fewer “external” acid sites, thus showing lower activity than IPC-2/IPC-4 catalysts, even though they have the same textural properties and total concentration of acid sites. The findings of this study not only provide evidence of the direct effects of the location of acid sites and micropore structure of zeolites on their catalytic performance but also show that the use of Al-IPC-*n* as model catalysts in important acid-catalyzed reactions helps to explain the fundamental structure–activity relationship and to improve existing catalytic processes.

■ ASSOCIATED CONTENT

Supporting Information

The Supporting Information is available free of charge on the ACS Publications website at DOI: 10.1021/acscatal.9b00950.

N₂ adsorption and desorption isotherms and ²⁷Al MAS NMR spectra of aluminated IPC-7 zeolites washed with 0.01 M HCl at different times; FTIR spectra of IPC-2, IPC-4, and IPC-6 before adsorption and after adsorption of acetonitrile-, quinoline-, or quinoline-preadsorbed followed by acetonitrile; scheme of the average structure of IPC-6; physicochemical properties of the IPC-2/IPC-4 composite and IPC-6 catalyst (PDF)

■ AUTHOR INFORMATION

Corresponding Authors

*E-mail: mariya.shamzhy@natur.cuni.cz.

*E-mail: maksym.opanenko@natur.cuni.cz.

ORCID

Shashikant A. Kadam: 0000-0002-4298-4074

Mariya Shamzhy: 0000-0002-1979-6817

Notes

The authors declare no competing financial interest.

■ ACKNOWLEDGMENTS

M.S. and M.O. thank the Primus Research Program of the Charles University (project number PRIMUS/17/SCI/22 “Soluble zeolites”) and the Neuron funding program (project number 31/2017). J.Č. acknowledges the support of the Czech Science Foundation through the project EXPRO (19-27551X). We acknowledge OP VVV “Excellent Research Teams” Project No. CZ.02.1.01/0.0/0.0/15_003/0000417-CUCAM.

■ REFERENCES

- (1) Vogt, E. T. C.; Weckhuysen, B. M. Fluid Catalytic Cracking: Recent Developments on the Grand Old Lady of Zeolite Catalysis. *Chem. Soc. Rev.* **2015**, *44*, 7342–7370.
- (2) Corma, A.; Huber, G. W.; Sauvanaud, L.; O’connor, P. Processing Biomass-derived Oxygenates in the Oil Refinery: Catalytic Cracking (FCC) Reaction Pathways and Role of Catalyst. *J. Catal.* **2007**, *247*, 307–327.
- (3) Cheng, K.; Kang, J.; Huang, S.; You, Z.; Zhang, Q.; Ding, J.; Wang, Y. Mesoporous Beta Zeolite-Supported Ruthenium Nanoparticles for Selective Conversion of Synthesis Gas to C₅–C₁₁ Isoparaffins. *ACS Catal.* **2012**, *2*, 441–449.
- (4) Xue, Y.; Li, J.; Wang, S.; Cui, X.; Dong, M.; Wang, G.; Fan, W. Co-reaction of Methanol with Butene over a High-silica H-ZSM-5 Catalyst. *J. Catal.* **2018**, *367*, 315–325.
- (5) Čejka, J.; Morris, R. E.; Nachtigall, P., Eds. *Zeolites in Catalysis: Properties and Applications*; Royal Society of Chemistry: UK, 2017; Chapter 11, pp 409–440.

- (6) Opanasenko, M. V.; Roth, W. J.; Čejka, J. Two-dimensional Zeolites in Catalysis: Current Status and Perspectives. *Catal. Sci. Technol.* **2016**, *6*, 2467–2484.
- (7) Simon-Masseron, A.; Marques, J. P.; Lopes, J. M.; Ribeiro, F. R.; Gener, I.; Guisnet, M. Influence of the Si/Al Ratio and Crystal Size on the Acidity and Activity of HBEA Zeolites. *Appl. Catal., A* **2007**, *316*, 75–82.
- (8) Zhang, J.; Zhao, C. Development of a Bimetallic Pd-Ni/HZSM-5 Catalyst for the Tandem Limonene Dehydrogenation and Fatty Acid Deoxygenation to Alkanes and Arenes for Use as Biojet Fuel. *ACS Catal.* **2016**, *6*, 4512–4525.
- (9) Peters, T. A.; Benes, N. E.; Holmen, A.; Keurentjes, J. T. Comparison of Commercial Solid Acid Catalysts for the Esterification of Acetic Acid with Butanol. *Appl. Catal., A* **2006**, *297*, 182–188.
- (10) Dusselier, M.; Deimund, M. A.; Schmidt, J. E.; Davis, M. E. Methanol-to-Olefins Catalysis with Hydrothermally Treated Zeolite SSZ-39. *ACS Catal.* **2015**, *5*, 6078–6085.
- (11) Eliášová, P.; Opanasenko, M.; Wheatley, P. S.; Shamzhy, M.; Mazur, M.; Nachtigall, P.; Roth, W. J.; Morris, R. E.; Čejka, J. The ADOR Mechanism for the Synthesis of New Zeolites. *Chem. Soc. Rev.* **2015**, *44*, 7177–7206.
- (12) Morris, S. A.; Bignami, G. P.; Tian, Y.; Navarro, M.; Firth, D. S.; Čejka, J.; Wheatley, P. S.; Dawson, D. M.; Slawinski, W. A.; Wragg, D. S.; Morris, R. E. In Situ Solid-state NMR and XRD Studies of the ADOR Process and the Unusual Structure of Zeolite IPC-6. *Nat. Chem.* **2017**, *9*, 1012–1018.
- (13) Bignami, G. P. M.; Dawson, D. M.; Seymour, V. R.; Wheatley, P. S.; Morris, R. E.; Ashbrook, S. E. Synthesis, Isotopic Enrichment, and Solid-State NMR Characterization of Zeolites Derived from the Assembly, Disassembly, Organization, Reassembly Process. *J. Am. Chem. Soc.* **2017**, *139*, 5140–5148.
- (14) Chlubná, P.; Tian, Y.; Pinar, A. B.; Kubů, M.; Čejka, J.; Morris, R. E. The Assembly-Disassembly-Organization-Reassembly Mechanism for 3D-2D-3D Transformation of Germanosilicate IWW Zeolite. *Angew. Chem., Int. Ed.* **2014**, *53*, 7048–7052.
- (15) Kasneryk, V.; Shamzhy, M.; Opanasenko, M.; Wheatley, P. S.; Morris, S. A.; Russell, S. E.; Mayoral, A.; Trachta, M.; Čejka, J.; Morris, R. E. Expansion of the ADOR Strategy for the Synthesis of Zeolites: The Synthesis of IPC-12 from Zeolite UOV. *Angew. Chem., Int. Ed.* **2017**, *56*, 4324–4327.
- (16) Firth, D. S.; Morris, S. A.; Wheatley, P. S.; Russell, S. E.; Slawinski, W. A. M. Z.; Dawson, D. M.; Mayoral, A.; Opanasenko, M.; Pološij, M.; Čejka, J.; Nachtigall, P.; Morris, R. E. Assembly–Disassembly–Organization–Reassembly Synthesis of Zeolites Based on cfi-Type Layers. *Chem. Mater.* **2017**, *29*, 5605–5611.
- (17) Roth, W. J.; Nachtigall, P.; Morris, R. E.; Wheatley, P. S.; Seymour, V. R.; Ashbrook, S. E.; Chlubná, P.; Grajciar, L.; Pološij, M.; Zukal, A.; Shvets, O.; Čejka, J. A Family of Zeolites with Controlled Pore Size Prepared Using a Top-down Method. *Nat. Chem.* **2013**, *5*, 628–633.
- (18) Wheatley, P. S.; Chlubná, P.; Greer, H.; Zhou, W.; Seymour, V. R.; Dawson, D. M.; Ashbrook, S. E.; Pinar, A. B.; McCusker, L. B.; Opanasenko, M.; Čejka, J.; Morris, R. E. Zeolites with Continuously Tuneable Porosity. *Angew. Chem., Int. Ed.* **2014**, *53*, 13210–13214.
- (19) Mazur, M.; Wheatley, P.; Navarro, M.; Roth, W. J.; Mayoral, A.; Eliášová, P.; Nachtigall, P.; Čejka, J.; Morris, R. E.; Pološij, M. Synthesis of 'Unfeasible' Zeolites. *Nat. Chem.* **2016**, *8*, 58–62.
- (20) Roth, W. J.; Shvets, O. V.; Shamzhy, M.; Chlubná, P.; Kubů, M.; Nachtigall, P.; Čejka, J. Postsynthesis Transformation of Three-dimensional Framework into a Lamellar Zeolite with Modifiable Architecture. *J. Am. Chem. Soc.* **2011**, *133*, 6130–6133.
- (21) Paillaud, J. L.; Harbuzaru, B.; Patarin, J.; Bats, N. Extra-large-pore Zeolites with Two-dimensional Channels Formed by 14 and 12 Rings. *Science* **2004**, *304*, 990–992.
- (22) Corma, A.; Diaz-Caban, M. J.; Rey, F.; Nicolopoulos, S.; Boualaya, K. ITQ-15: The First Ultralarge Pore Zeolite with a Bidirectional Pore System Formed by Intersecting 14- and 12-ring Channels, and Its Catalytic Implications. *Chem. Commun.* **2004**, *12*, 1356–1357.
- (23) Verheyen, E.; Joos, L.; Van Havenbergh, K.; Breynaert, E.; Kasian, N.; Gobechiya, E.; Houthoofd, K.; Martineau, C.; Hinterstein, M.; Taulelle, F.; Van Speybroeck, V. Design of Zeolite by Inverse Sigma Transformation. *Nat. Mater.* **2012**, *11*, 1059–1064.
- (24) Jagiello, J.; Sterling, M.; Eliášová, P.; Opanasenko, M.; Zukal, A.; Morris, R. E.; Navaro, M.; Mayoral, A.; Crivelli, P.; Warringham, R.; Mitchell, S.; Pérez-Ramírez, J.; Čejka, J. Structural Analysis of IPC Zeolites and Related Materials Using Positron Annihilation Spectroscopy and High-resolution Argon Adsorption. *Phys. Chem. Chem. Phys.* **2016**, *18*, 15269–15277.
- (25) Zukal, A.; Shamzhy, M.; Kubů, M.; Čejka, J. The Effect of Pore Size Dimensions in Isoreticular Zeolites on Carbon Dioxide Adsorption Heats. *J. CO₂ Util.* **2018**, *24*, 157–163.
- (26) Přeč, J.; Morris, R. E.; Čejka, J. Selective Oxidation of Bulky Organic Sulphides over Layered Titanosilicate Catalysts. *Catal. Sci. Technol.* **2016**, *6*, 2775–2786.
- (27) Přeč, J.; Čejka, J. UTL Titanosilicate: An Extra-large Pore Epoxidation Catalyst with Tunable Textural Properties. *Catal. Today* **2016**, *277*, 2–8.
- (28) Žilková, N.; Eliášová, P.; Al-Khattaf, S.; Morris, R. E.; Mazur, M.; Čejka, J. The Effect of UTL Layer Connectivity in Isoreticular Zeolites on the Catalytic Performance in Toluene Alkylation. *Catal. Today* **2016**, *277*, 55–60.
- (29) Dědeček, J.; Sobalík, Z.; Wichterlová, B. Siting and Distribution of Framework Aluminium Atoms in Silicon-Rich Zeolites and Impact on Catalysis. *Catal. Rev.: Sci. Eng.* **2012**, *54*, 135–223.
- (30) Jones, A. J.; Carr, R. T.; Zones, S. L.; Iglesia, E. Acid Strength and Solvation in Catalysis by MFI Zeolites and Effects of the Identity, Concentration and Location of Framework Heteroatoms. *J. Catal.* **2014**, *312*, 58–68.
- (31) Vjunov, A.; Fulton, J. L.; Huthwelker, T.; Pin, S.; Mei, D.; Schenter, G. K.; Govind, N.; Camaioni, D. M.; Hu, J. Z.; Lercher, J. A. Quantitatively Probing the Al Distribution in Zeolites. *J. Am. Chem. Soc.* **2014**, *136*, 8296–8306.
- (32) Chen, J.; Liang, T.; Li, J.; Wang, S.; Qin, Z.; Wang, P.; Huang, L.; Fan, W.; Wang, J. Regulation of Framework Aluminum Siting and Acid Distribution in H-MCM-22 by Boron Incorporation and Its Effect on the Catalytic Performance in Methanol to Hydrocarbons. *ACS Catal.* **2016**, *6*, 2299–2313.
- (33) Matsunaga, Y.; Yamazaki, H.; Imai, H.; Yokoi, T.; Tatsumi, T.; Kondo, J. N. Hexamethyleneimine and Pivalonitrile as Location Probe Molecules of Lewis Acid Sites on MWW-type Zeolites. *Microporous Mesoporous Mater.* **2015**, *206*, 86–94.
- (34) Onida, B.; Geobaldo, F.; Testa, F.; Crea, F.; Garrone, E. FTIR Investigation of the Interaction at 77 K of Diatomic Molecular Probes on MCM-22 Zeolite. *Microporous Mesoporous Mater.* **1999**, *30*, 119–127.
- (35) Wang, S.; Wang, P.; Qin, Z.; Chen, Y.; Dong, M.; Li, J.; Zhang, K.; Liu, P.; Wang, J.; Fan, W. Relation of Catalytic Performance to the Aluminum Siting of Acidic Zeolites in the Conversion of Methanol to Olefins, Viewed via a Comparison between ZSM-5 and ZSM-11. *ACS Catal.* **2018**, *8*, 5485–5505.
- (36) Liang, T.; Chen, J.; Qin, Z.; Li, J.; Wang, P.; Wang, S.; Wang, G.; Dong, M.; Fan, W.; Wang, J. Conversion of Methanol to Olefins over H-ZSM-5 Zeolite: Reaction Pathway Is Related to the Framework Aluminum Siting. *ACS Catal.* **2016**, *6*, 7311–7325.
- (37) Wang, S.; Li, S.; Zhang, L.; Qin, Z.; Dong, M.; Li, J.; Wang, J.; Fan, W. Insight into the Effect of Incorporation of Boron into ZSM-11 on Its Catalytic Performance for Conversion of Methanol to Olefins. *Catal. Sci. Technol.* **2017**, *7*, 4766–4779.
- (38) Shvets, O. V.; Zukal, A.; Kasian, N.; Žilková, N.; Čejka, J. The Role of Crystallization Parameters for the Synthesis of Germanosilicate with UTL Topology. *Chem. - Eur. J.* **2008**, *14*, 10134–10140.
- (39) Shamzhy, M. V.; Shvets, O. V.; Opanasenko, M. V.; Yaremov, P. S.; Sarkisyan, L. G.; Chlubná, P.; Čejka, J. Synthesis of Isomorphously Substituted Extra-large Pore UTL Zeolites. *J. Mater. Chem.* **2012**, *22*, 15793–15803.

(40) Wichterlová, B.; Tvarůšková, Z.; Sobalík, Z.; Sarv, P. Determination and Properties of Acid Sites in H-ferrierite: A Comparison of Ferrierite and MFI Structures. *Microporous Mesoporous Mater.* **1998**, *24*, 223–233.

(41) Lawton, S. L.; Leonowicz, M. E.; Partridge, R. D.; Chu, P.; Rubin, M. K. Twelve-ring Pockets on the External Surface of MCM-22 Crystals. *Microporous Mesoporous Mater.* **1998**, *23*, 109–117.

(42) Šteková, M.; Kubů, M.; Shamzhy, M.; Musilová, Z.; Čejka, J. α -Pinene Oxide Isomerization: Role of Zeolite Structure and Acidity in the Selective Synthesis of Campholenic Aldehyde. *Catal. Sci. Technol.* **2018**, *8*, 2488–2501.

(43) Corma, A.; Fornés, V.; Rey, F. Quinoline as a Probe Molecule for Determination of External Brønsted and Lewis Acidity in Zeolites. *Zeolites* **1993**, *13*, 56–59.

(44) Chiang, H.; Bhan, A. Catalytic Consequences of Hydroxyl Group Location on the Rate and Mechanism of Parallel Dehydration Reactions of Ethanol over Acidic Zeolites. *J. Catal.* **2010**, *271*, 251–261.

(45) Kadam, S. A.; Shamzhy, M. V. IR Operando Study of Ethanol Dehydration over MFI zeolite. *Catal. Today* **2018**, *304*, 51–57.

(46) Kadam, S. A.; Shamzhy, M. V. IR Operando Study of Ethanol Dehydration over MFI Zeolites: Structure-Activity Relationships. *J. Phys. Chem. C* **2018**, *122*, 24055–24067.

(47) Di Iorio, J. R.; Nimlos, C. T.; Gounder, R. Introducing Catalytic Diversity into Single-Site Chabazite Zeolites of Fixed Composition via Synthetic Control of Active Site Proximity. *ACS Catal.* **2017**, *7* (10), 6663–6674.

(48) Carr, R. T.; Neurock, M.; Iglesia, E. Catalytic Consequences of Acid Strength in the Conversion of Methanol to Dimethyl ether. *J. Catal.* **2011**, *278*, 78–93.

(49) Jones, A. J.; Zones, S. L.; Iglesia, E. Implications of Transition State Confinement within Small Voids for Acid Catalysis. *J. Phys. Chem. C* **2014**, *118*, 17787–17800.

(50) Naik, S. G. R.; Patel, B. K. Tetrabutylammonium Tribromide (TBATB)-promoted Tetrahydropyranylation/depyranylation of Alcohols. *Tetrahedron Lett.* **2001**, *42*, 7679–7681.

(51) Chandrasekhar, S. T. M.; Reddy, Y. R.; Mohapatra, S.; Rao, C. R.; Reddy, K. V. TaCl₅-silicagel and TaCl₅ as New Lewis Acid Systems for Selective Tetrahydropyranylation of Alcohols and Thioacetalisation, Trimerisation and Aldolisation of Aldehydes. *Tetrahedron* **1997**, *53*, 14997–15004.



Novel approach towards Al-rich AFI for catalytic application

Yong Zhou^{a,b}, Naděžda Žilková^a, Mariya Shamzhy^b, Yamini Avadhut^c, Martin Hartmann^c, Jiří Čejka^b, Maksym Opanasenko^{b,*}^a J. Heyrovsky Institute of Physical Chemistry, Czech Academy of Sciences, Dolejškova 3, 182 23, Prague 8, Czech Republic^b Department of Physical and Macromolecular Chemistry, Faculty of Science, Charles University in Prague, Hlavova 8, 128 43, Prague 2, Czech Republic^c Erlangen Catalysis Resource Center, Friedrich-Alexander-Universität Erlangen-Nürnberg, Egerlandstr. 3, 91058, Erlangen, Germany

ARTICLE INFO

Keywords:

AFI
Zeolite
Germanosilicate
Isomorphous substitution
Toluene alkylation

ABSTRACT

A new germanosilicate structural analogue of AFI zeolite (Ge-AFI) was hydrothermally synthesized. One- and two-step aluminations of the Ge-AFI zeolites were used to modify their structure and acidic properties traced using XRD, N₂ adsorption, ICP-OES, ²⁷Al NMR, and FTIR spectroscopy. Two-step aluminated sample (deGe-Al-AFI) provided a higher Al content, stronger acid sites and a higher micropore volume than one-step aluminated sample (Al-AFI). Extensive evaluation of the catalytic performance of these AFI zeolites compared with reference conventional zeolite catalysts for alkylation of toluene with isopropyl alcohol showed that deGe-Al-AFI exhibited relatively high toluene conversion and selectivity to valuable *p*-cymene due to the optimized textural and acidic properties.

1. Introduction

Synthesis of zeolites with large (12-ring) and extra-large (> 12-ring) pores is of a great interest and importance due to their ability to accommodate bulky molecules in adsorption and catalysis [1–3]. As an example, zeolite and zeotype materials with the AFI framework type have been investigated in such as shape-selective catalysis and gas separation [4–8] because of their unique one-dimensional parallel 12-ring pore opening of 7.3 Å [9].

The synthesis of the pure silica AFI zeolite (SSZ-24) was reported over 20 years ago by Zones et al. [10], however, the direct hydrothermal crystallization of Al containing SSZ-24 has never been achieved. Later, the success in the synthesis of borosilicate SSZ-24 provided a chance to incorporate heteroatoms, e.g. Al and Fe, into the SSZ-24 framework for preparation of the desirable shape-selective catalysts [5,11,12]. B-SSZ-24 can be synthesized either using a calcined borosilicate Beta as the boron and silica sources [11] or using N(16)-methylsperminium as structure directing agent (SDA) [12]. However, only a limited amount of Al (Si/Al > 63) or Ti (Si/Ti > 200) can be incorporated into the AFI framework when using B-SSZ-24 precursor by isomorphous substitution [7,13]. In contrast to the conversion of B-Beta into B-SSZ-24 followed by aluminations, Hiroyoshi et al. reported the hydrothermal synthesis of Al-SSZ-24 with Si/Al = 70 from Al-Beta zeolite precursor [14]. In order to improve the potential of substituted

SSZ-24 zeolites as catalyst increasing the content of active sites, the new method to prepare heteroatom-containing SSZ-24 is still highly desirable.

Over the last decade, many new large- and extra-large- pore zeolites have been synthesized in the germanosilicate form [15–18]. Germanium acts as inorganic structure-directing-agent (SDA) stabilizing the formation of small building units, e.g. double four rings (d4r) or double three rings (d3r), having high geometric constraints [19]. On the other hand, germanosilicates possess hydrolytic lability of Ge–O bonds, which stimulated researchers developed methods to incorporate heteroatoms, e.g. B, Al, Ga, Ti, Sn, into the frameworks of germanosilicates by post-synthetic synthesis, such as BEC [20], UTL [21–23], IWW and ITH [21], IWR [24], and ITQ-33 [25]. Such isomorphous substitution with trivalent or tetravalent heteroatoms into the zeolite framework not only stabilizes the zeolite structure but also introduces the active sites into the frameworks. Therefore, the synthesis of germanosilicate AFI zeolite followed by the post-synthetic substitution could be a desirable way to obtain AFI zeolite with reasonably high content of catalytically active sites.

In the present work, we report the synthesis of a new germanosilicate SSZ-24 (Ge-AFI) zeolite and utilization of this germanosilicate for post-synthetic isomorphous substitution via either one-step or two-step aluminations procedures. The catalytic properties of aluminated AFI materials were evaluated in the alkylation of toluene with isopropyl

* Corresponding author at: Department of Physical and Macromolecular Chemistry, Faculty of Science, Charles University in Prague, Hlavova 8, 128 43, Prague 2, Czech Republic.

E-mail address: maksym.opanasenko@natur.cuni.cz (M. Opanasenko).

<https://doi.org/10.1016/j.apcata.2019.03.015>

Received 12 December 2018; Received in revised form 11 March 2019; Accepted 19 March 2019

Available online 22 March 2019

0926-860X/ © 2019 Elsevier B.V. All rights reserved.

alcohol.

2. Experimental

2.1. Materials and synthesis

2.1.1. Materials

1,5-dibromopentane (97%, Sigma Aldrich), *cis*-2,6-dimethylpiperidine (98%, Sigma Aldrich), NaOH (98%, Lanchner), Sodium sulfate (Sigma Aldrich), Chloroform (Lanchner), Diethyl ether (Lanchner), Ambersep® 900(OH) (Alfa Aesar), Germanium oxide (99.99%, Sigma Aldrich), Cab-O-Sil M-5 (Supelco Analytical), Aluminum nitrate non-hydrated (99.4%, Lanner), Hydrochloric acid (37 wt. % in H₂O, Lanchner).

2.1.2. Synthesis

2.1.2.1. Structure directing agent (SDA). The 7, 11-dimethyl-6-azoniaspiro [5.6] undecane was synthesized with the method similar to that described in the literature [26]. 140 ml of distilled water, 5.68 g NaOH, and 32.65 g 1, 5-dibromopentane were mixed in a glass flask. Then, 16.07 g of (2R, 6S)-2, 6-dimethylpiperidine was added dropwise under reflux. The mixture was under very intensive stirring to prepare a milk-like suspension and then cooled in an ice bath. Another small amount of NaOH was added very slowly under vigorous stirring and cooling by ice until the appearance of the oil products. Further stirring for 1 h led to the formation of the crystalline phase, which was recovered by filtration and extracted with 300 ml chloroform. The organic fractions were dried using anhydrous sodium sulfate and partially evaporated. The ammonium salt was precipitated and washed out with diethyl ether. The salt was converted into hydroxide form by ion exchange with Ambersep® 900(OH) anion exchange resin.

2.1.2.2. Ge-AFI. The germanosilicate AFI zeolite (referred to as Ge-AFI) was synthesized from a gel using 7, 11-dimethyl-6-azoniaspiro [5.6] undecane as SDA with a molar composition: 0.96 SiO₂ : 0.24 GeO₂ : 0.4 SDA : 30 H₂O. The gel was prepared by dissolving germanium oxide in the solution of SDAOH followed by addition of silica into the solution and the mixture was stirred at room temperature for 30 min. Hydrothermal crystallization was conducted at 175 °C for 7 days under agitation.

The ranges of compositions yielding the germanosilicate AFI can be varied:

$$0.9 - 0.96 \text{ SiO}_2 : 0.24 - 0.3 \text{ GeO}_2 : 0.4 \text{ SDA} : 30 \text{ H}_2\text{O}.$$

The solid products were recovered by filtration with water and then dry at 65 °C overnight. To remove the SDA from the zeolites, the as-synthesized samples were calcined in air at 550 °C for 6 h.

2.1.2.3. Al-AFI. Al containing AFI catalyst synthesized through one-step alumination of calcined Ge-AFI is referred to as Al-AFI. 1 g of calcined zeolite was treated with 100 ml of 1 M Al(NO₃)₃ solution at 80 °C for 48 h. The aluminated sample was subsequently centrifuged and washed with 0.01 M HCl and water and then dried at 65 °C overnight.

2.1.2.4. deGe-Al-AFI. Al containing AFI catalyst synthesized through two-step alumination of calcined Ge-AFI is referred to as deGe-Al-AFI. 1 g of calcined zeolite was treated with 100 ml of 0.1 M HCl solution at 80 °C for 16 h. After the treatment, the zeolite was centrifuged and washed with water to pH = 7. The alumination was conducted by addition of 100 ml of 1 M Al(NO₃)₃ solution at 80 °C for 48 h. The aluminated sample were subsequently centrifuged and washed with 0.01 M HCl and water and then dried at 65 °C overnight.

All the aluminated samples were calcined at 450 °C for 4 h prior further characterization.

2.2. Characterization

The structure and crystallinity of zeolites were determined by powder X-ray diffraction (XRD) using a Bruker AXS D8 Advance diffractometer with Cu K α radiation in Bragg-Brentano geometry. The chemical composition was determined an inductively coupled plasma-optical emission spectrometry (ICP/OES) (ThermoScientific Icap7000). Crystal size and shape of all the samples were assessed using a JSM-5500LV microscope. Nitrogen adsorption measurements were carried out on a Micromeritics GEMINI II 2370 volumetric Surface Area Analyzer at -196 °C to determine BET area and pore volume.

Concentration of Lewis (c_L) and Brønsted (c_B) acid sites was determined after adsorption of pyridine (PyR) by Fourier-transform infrared spectroscopy (FTIR) on Nicolet 6700 FTIR with MCT/B detector. Zeolites were pressed into self-supporting wafers with a density of 8.0–12 mg/cm² and activated in situ at 450 °C overnight. Pyridine adsorption was carried out at 150 °C for 20 min at partial pressure 600–800 Pa, followed by desorption for 20 min. Before adsorption pyridine was degassed by freezing and thawing cycles. All spectra were recorded with a resolution of 4 cm⁻¹ by collecting 128 scans for a single spectrum at room temperature. Spectra were calculated on wafer density of 10 mg cm⁻². Concentration of c_L and c_B were evaluated from the integral intensities of bands at 1454 cm⁻¹ (c_L) and at 1545 cm⁻¹ (c_B) using molar absorption coefficients, $\epsilon(L) = 2.22 \text{ cm} \mu\text{mol}^{-1}$, and $\epsilon(B) = 1.67 \text{ cm} \mu\text{mol}^{-1}$ [27]. For the determination of the strength of different acid sites, desorption of pyridine was carried out at 150, 250, 350 and 450 °C followed by FTIR measurements. A relatively large probe molecule 2,6-di-tert-butyl-pyridine (DTBP) was used to determine the accessibility of acid sites within prepared zeolites [28]. The adsorption of DTBP took place at 150 °C and at equilibrium probe vapour pressure with the zeolite wafer for 15 min. Desorption proceeded at the same temperature for 1 h followed by collection of spectra at room temperature. Molar absorption coefficient from Ref [27], was used for evaluation of c_B accessible for DTBP using integral intensity of absorption band ca. 1530 cm⁻¹.

The solid state ²⁷Al nuclear magnetic resonance (NMR) spectra were recorded under magic angle spinning (MAS) with a commercial 3.2 mm triple resonance MAS probe spinning at 15 kHz on an Agilent DD2 500WB spectrometer operating at a resonance frequency of 130.24 MHz.

2.2.1. Catalytic test

Toluene alkylation with isopropyl alcohol was investigated in a vapor phase continuous down-flow glass micro-reactor with a fixed bed of catalyst under atmospheric pressure. Before the catalytic run, all the zeolite catalysts studied were activated at 500 °C in nitrogen stream for 120 min. The reaction was performed at 250 °C with toluene to isopropyl alcohol (Tol/*i*-PROH) molar ratio of 9.6 and weight hour space velocity (WHSV) based on toluene equal to 10 h⁻¹. The reaction products were analyzed using an Agilent 6890 Plus “on-line” gas chromatograph with flame ionization detector and a high-resolution capillary DB-5 column (length 50 m, diameter 0.32 mm, and film thickness 1 μm). After 15 min of the time-on-stream (T-O-S), the first analysis was done, followed by further sampling of the reaction products at approx. 50 min interval.

3. Results and discussion

3.1. Synthesis and characterization of aluminated AFI zeolites by using Ge-AFI as precursors

Germanosilicate Ge-SSZ-24 (Ge-AFI) with Si/Ge of 8.1 in the framework (Table 1) was prepared under hydrothermal conditions using 7, 11-dimethyl-6-azoniaspiro [5.6] undecane as SDA in this study. The synthesis of Ge-AFI is sensitive to the Ge content in the gel mixture (Fig. S1). At Si/Ge ratio ≤ 2 , germanosilicate UTL is the main phase, while at

Table 1
Physicochemical and textural properties of Ge- or Al-zeolites under investigation.

Catalyst	Pore system dimension	Si/Ge ^a	Si/Al ^a	S _{BET} ^b /m ² g ⁻¹	V _{tot} ^c /cm ³ g ⁻¹	V _{micro} ^c /cm ³ g ⁻¹
Ge-AFI	1 D	8.1	–	306	0.26	0.10
Al-AFI	–	25	53	128	0.19	0.02
deGe-AFI	–	22	–	330	0.27	0.11
deGe-Al-AFI	–	38	29	356	0.24	0.12
MTW	1D	–	52	296	0.22	0.10
IPC-2	2D	–	48	390	0.20	0.16
Beta	3D	–	23	619	0.35	0.25

^a Measured by ICP/OES. ^b Specific surface area (BET) given by N₂ adsorption at –196 °C. ^c Calculated by t-plot method.

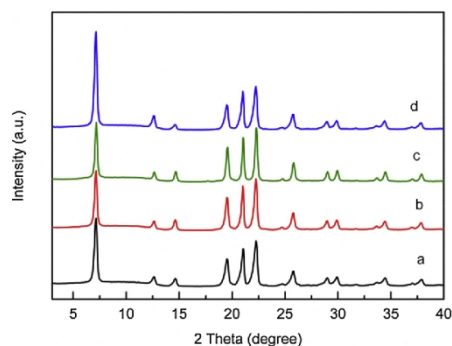


Fig. 1. XRD patterns of Ge-AFI (a), Al-AFI (b), deGe-AFI (c), and deGe-Al-AFI (d) zeolites.

Si/Ge ratio ≥ 3 , pure Ge-AFI could be obtained. For further incorporation of Al into AFI zeolite, direct aluminations (denoted as Al-AFI) and two-step degermanation-aluminations (deGe-Al-AFI) were performed in order to evaluate the necessity for the careful acidic leaching of Ge prior the introduction of Al into the framework.

The structures of starting, intermediate and final AFI samples were investigated with XRD. Fig. 1 shows that the calcined Ge-AFI had high crystallinity and no impurities at detectable level. Both aluminated AFI samples obtained by the one- or two-step aluminations retained topology typical for AFI (Fig. 1). The crystals of synthesized Ge-AFI precursor have the needle shape (3 μm \times 0.2 μm) and form aggregates of several μm size (Fig. 2, a). It is worth to note that the morphology of obtained AFI zeolite significantly differs from that of B-SSZ-24 having much larger hexagonal crystals [12]. This feature of Ge-AFI can potentially provide more efficient post-synthesis isomorphous substitution due to the decreased diffusional restrictions in tiny needle-like crystals in comparison with bulky ones. After post-synthetic aluminations, needle-shape crystal morphology typical for Ge-AFI was preserved in the deGe-Al-AFI and Al-AFI samples (Fig. 2b and c). These results indicate the

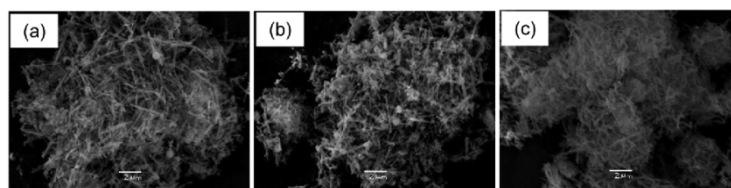


Fig. 2. SEM images of Ge-AFI (a), deGe-Al-AFI (b), and Al-AFI (c) zeolites.

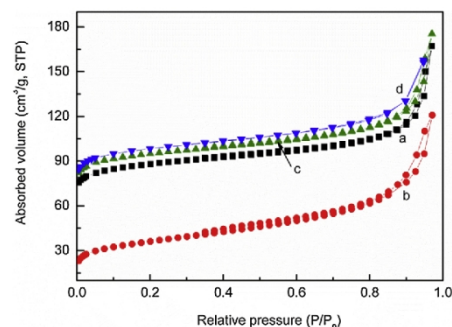


Fig. 3. N₂ adsorption and desorption isotherms of the calcined Ge-AFI precursor (a), Al-AFI (b), deGe-AFI (c), and deGe-Al-AFI (d) samples at –196 °C.

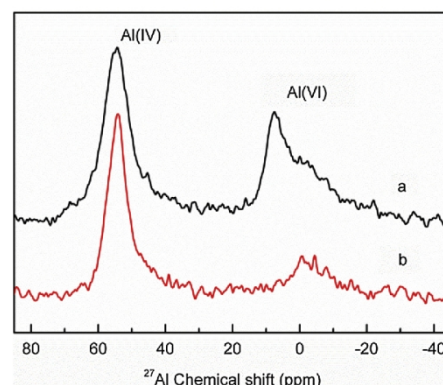


Fig. 4. ²⁷Al NMR spectra of Al-AFI (a) and deGe-Al-AFI (b).

applied aluminations have almost no impact on the crystal structure and morphology of substituted AFI zeolites.

All AFI samples showed similar and typical type I adsorption/desorption isotherms (Fig. 3) with gradual increase in the adsorbate uptake in the range 0.1 – 0.9 p/p_0 probably due to the very small size of the crystals and an enhanced nitrogen uptake at high relative pressure $p/p_0 > 0.9$ may be ascribed to the existence of interparticle voids of different size generated from the disordered agglomeration of crystallites. Compared to the Ge-AFI precursor, Al-AFI sample demonstrated a significantly lower BET area and the pore volume (Table 1) that could be caused by the deposition of inorganic remnants in the pores of Al-AFI. The source of these residues can be either the former framework domains formed during leaching of Ge from the structure or aluminum-containing species formed during the treatment with Al(NO₃)₃ solution; however, they could not be traced by XRD because of small size of these

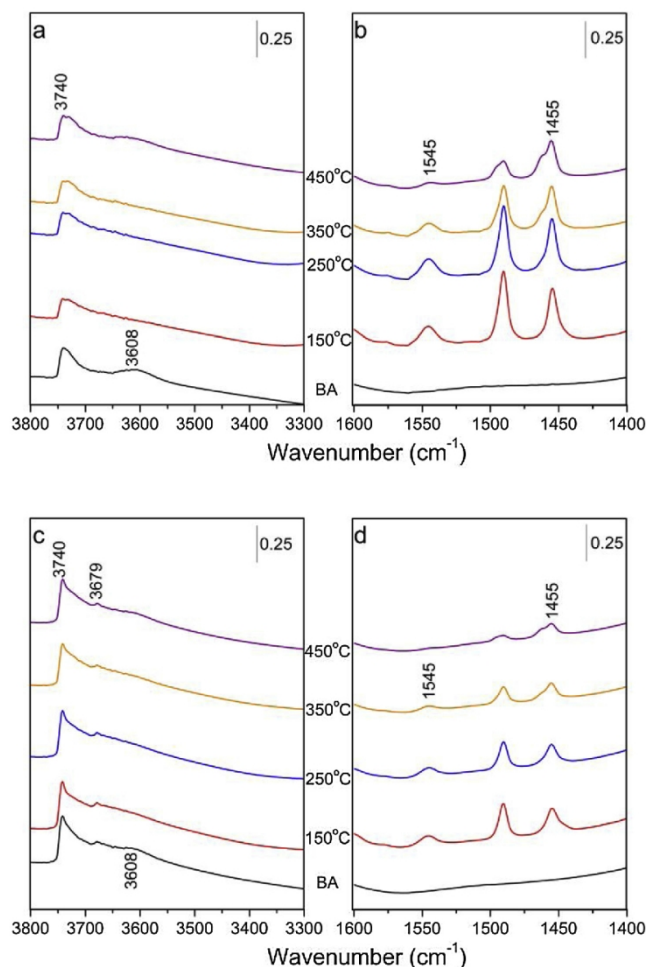


Fig. 5. FTIR spectra of (a, b) deGe-Al-AFI and (c, d) Al-AFI before (BA), and after pyridine adsorption, followed by desorption at 150 °C, 250 °C, 350 °C, and 450 °C.

Table 2
Acidic properties of catalysts determined by pyridine-IR at 150 °C.

Catalyst	Brønsted ^a /mmol g ⁻¹	Lewis ^b /mmol g ⁻¹	Total /mmol g ⁻¹	B/L ratio
Al-AFI	0.05	0.08	0.13	0.63
deGe-Al-AFI	0.11	0.15	0.26	0.73
MTW	0.11	0.03	0.14	3.67
IPC-2	0.13	0.12	0.25	1.08
Beta	0.33	0.19	0.52	1.74

^a Calculated from the area of the band located at around 1545 cm⁻¹. ^b Calculated from the area of the band located at around 1455 cm⁻¹.

species. On the other hand, textural characteristics of the sample obtained by two-step treatment were similar to that of Ge-AFI. Intermediate HCl-treated Ge-AFI sample (deGe-AFI) exhibited increased BET area (from 306 to 330 m² g⁻¹) and micropore volume (from 0.10 to 0.11 cm³ g⁻¹) (Table 1), which may be caused by removal of the Ge

species from the framework (in agreement with the chemical analysis showing the increase in the Si/Ge molar ratio from 8.1–22) and formation of the silanol nests. The following Al incorporation healed the defects and the resulting deGe-Al-AFI possessed a BET area and pore volume comparable to the parent Ge-AFI. These results suggest that the acid treatment prior to alumination is i) more beneficial for generation of hydroxyl nests by removal of germanium atoms from the framework, which weakens the steric hindrance for the insertion of Al isomorphously into the framework and ii) necessary to decrease the deposition of solid species that block the pores in final zeolite. According to the analysis of mesopore size distribution (Fig. S2), no significant changes in their characteristics were detected indicating that alumination affect mainly microporous system of AFI zeolite under conditions used.

To evaluate the state of Al atoms in the frameworks of zeolites obtained by different approaches, ²⁷Al NMR spectra of Al-AFI and deGe-Al-AFI were investigated (Fig. 4). The spectra consist of two groups of

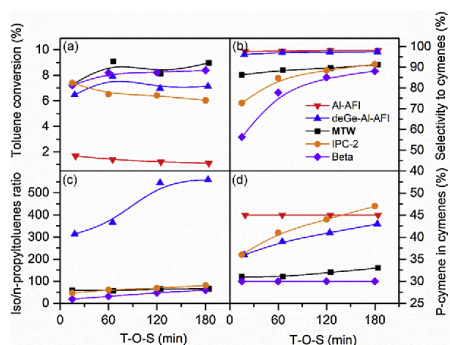


Fig. 6. Time-on-stream dependence of (a) toluene conversion, (b) selectivity to cymenes, (c) iso/*n*-propyltoluene ratio and (d) *para*-cymene selectivity in toluene alkylation with isopropyl alcohol over Al-AFI, deGe-Al-AFI, MTW, IPC-2 and Beta catalysts at 250 °C. Toluene to isopropyl alcohol (Tol/*i*-PrOH) molar ratio of 9.6 and WHSV based on toluene equal to 10 h⁻¹.

peaks centered around 55 and 0–10 ppm, which are assigned to tetrahedrally coordinated Al and extra-framework (penta-coordinated, octahedral or distorted octahedral) Al, respectively. deGe-Al-AFI possessed significantly lower fraction of extra-framework Al (about 10% of that in Al-AFI sample), which is consistent with the adsorption results and further confirms the necessity of an additional degermanation step prior to alumination, maybe the large amount of extra framework Al as pore blockage led to decrease in the pore volume in Al-AFI sample. Although, the ²⁷Al NMR spectra indicated the presence of extra framework Al, Al³⁺ is mainly incorporated into the tetrahedral framework positions by both alumination procedures.

In full agreement with ²⁷Al NMR results, FTIR spectrum of Al-AFI showed the band at 3679 cm⁻¹ attributed to Al–O–H groups of small non-acidic extra-framework aluminum species [29,30] (Fig. 5c), while both Al-AFI and deGe-Al-AFI possess the bands at 3740 and 3608 cm⁻¹ assigned to silanol and bridging hydroxyl =Si–(OH)–Al= groups [31] (Fig. 5a,c). To provide a detailed information about the type, amount, and strength of acid sites in deGe-Al-AFI and Al-AFI, FTIR spectroscopy of adsorbed pyridine was used. After pyridine adsorption, the intensities of the bands ca. 3740 and 3679 cm⁻¹ remained almost unchanged, while the band at 3608 cm⁻¹ assigned to bridging hydroxyl groups of acid character disappeared, evidencing the accessibility of all Brønsted acid centers for pyridine in the investigated samples. On the other hand, the adsorption of pyridine in Al-AFI and deGe-Al-AFI was accompanied with the appearance of a typical set of adsorption bands in the region 1400–1600 cm⁻¹ attributed to the probe molecule interacting either with Lewis or Brønsted acid sites. Fig. 5 shows the evolution of the absorption bands centered around 1455 and 1545 cm⁻¹ (related to pyridine molecules adsorbed on the Lewis and Brønsted acid sites, respectively) after desorption of pyridine from

deGe-Al-AFI (Fig. 5b) and Al-AFI (Fig. 5d) zeolites at different temperatures. The fraction of strong acid sites (calculated as the amount of pyridine molecules remaining adsorbed after heating at 623 K) was higher for deGe-Al-AFI sample (70%) in comparison with Al-AFI (54%). Only low intensive bands at 1455 and 1545 cm⁻¹ can be seen in the spectra of Al-AFI when the desorption temperature was increased to 723 K. In addition, the acid sites located at the external surface were assessed with DTBP as probe molecule (Fig. S3) with the kinetic diameter of 0.79 nm [28], being higher than the diameter of 12-ring channels in AFI zeolite. Indeed, the adsorption of DTBP on either Al-AFI or deGe-Al-AFI does not remove, but only slightly decreases intensity of the band at 3608 cm⁻¹ corresponding to bridging hydroxyl groups, which indicates a small fraction of Brønsted acid centers are accessible for DTBP. The bands at 1616 and 1530 cm⁻¹ can be detected in the region of chemisorbed DTBP were attributed to the formation of DTBPpyH⁺ ions [28]. The absence of a band at 1545 cm⁻¹ confirms no dealkylation of the probe molecule used. Based on the integral intensity of absorption band ca. 1530 cm⁻¹, the concentration of acid sites at external surface of Al-AFI (0.01 mmol g⁻¹) was evaluated to be 3 times lower compared to deGe-Al-AFI (0.03 mmol g⁻¹).

3.2. Catalytic performance of aluminated AFI zeolites

Aromatic alkylation reactions are widely employed as model reactions for the characterization of zeolite structures. Their activity and selectivity can be correlated to the textural and acidic properties of zeolites. [32–36] The catalytic performance of two aluminated AFI zeolites in the alkylation of toluene with isopropyl alcohol was compared with conventional zeolites possessing pore entrances of a size similar to AFI (12-ring channels) but different pore connectivity: MTW with 1-dimensional (1D) pore system (12-ring), IPC-2 with intersecting 12- and 10-ring channels (2D) and Beta zeolite possessing 3-dimensional (3D) pore system with 12-ring windows (Tables 1,2, Fig. 6). For the reference zeolites (except Beta), the concentration of Brønsted acid sites responsible for catalytic activity in the alkylation reaction [32,37,38] was kept similar to that of the most promising deGe-Al-AFI (0.11–0.13 mmol g⁻¹) to exclude the influence of this parameter on the overall catalytic activity. The catalysts were compared in terms of i) toluene conversion; ii) selectivity to cymene isomers; iii) para-selectivity to *p*-cymene; iv) iso/*n*-propyl ratio in cymenes (Fig. 6 and Table 4). Toluene conversion decreased in the order MTW ≈ Beta > deGe-Al-AFI > IPC-2 > Al-AFI (Fig. 6a). This result agrees with the Brønsted/Lewis acid ratio (B/L ratio) in the catalysts investigated (Table 2). Alkylation of toluene with alcohols catalyzed by zeolites is commonly considered to proceed via carbonium ion mechanisms [37,38] and the Brønsted acid sites are active sites of the reaction [32]. Lewis acid centers can act as the additional adsorption sites [39] slowing down the overall rates of reactants/products diffusion. Therefore, lower B/L ratio leads to lower catalytic activities. In spite of 12-ring in IPC-2, smaller 10-ring channels cause diffusion limitations similar to that found for MFI zeolite [34]. Additionally, IPC-2 zeolite had the plate-like morphology and relatively large crystals (Fig. S4) which

Table 3

Catalyst activity and products distribution in the alkylation of toluene with isopropyl alcohol on catalysts under study after 13 min of T-O-S.

Catalyst	Toluene Conv. (%)	Products selectivity (%)					cymene Sel. (%)
		<i>p</i> -cymene	<i>o</i> -cymene	<i>m</i> -cymene	propyl toluene	other	
Al-AFI	1.7	43.8	22.0	31.8	0	2.4	97.6
deGe-Al-AFI	7.2	33.7	6.9	55.3	0.4	3.7	95.9
MTW	7.3	26.5	4.5	55.4	1.5	12.1	86.4
IPC-2	7.4	25.8	1.3	45.6	1.6	25.7	72.7
Beta	7.2	16.7	2.8	36.9	2.9	40.7	56.4

Reaction conditions: toluene / *i*-PrOH molar ratio = 9.6, catalyst = 0.14 g, temperature = 250 °C, TOS = 13 min.

Table 4
Catalyst activity and products distribution in the alkylation of toluene with isopropyl alcohol on catalysts under study after 184 min of T-O-S.

Catalyst	Toluene Conv. (%)	Products selectivity (%)					cymene Sel. (%)
		<i>p</i> -cymene	<i>o</i> -cymene	<i>m</i> -cymene	propyl toluene	other	
Al-AFI	1.1	43.9	24.6	30.0	0	1.5	98.5
deGe-Al-AFI	6.4	41.0	11.0	45.3	0.2	2.5	97.3
MTW	9.0	30.0	5.1	56.3	1.4	7.2	91.4
IPC-2	6.0	43.3	1.2	47.0	1.1	7.4	91.5
Beta	8.4	26.3	4.4	57.4	1.5	10.4	88.1

Reaction conditions: toluene / *i*-PrOH molar ratio = 9.6, catalyst = 0.14 g, temperature = 250 °C, TOS = 184 min.

can only be accessed from the rim of the crystal plates, this could also result in diffusion limitations and hampers the efficient use of the catalyst [35]. These may be the reason why deGe-Al-AFI (B/L = 0.73) outperforms the IPC-2 (B/L = 1.08). Al-AFI exhibited the lowest toluene conversion, its relatively poor catalytic activity is caused by a partial blockage of the pores during one-step alumination treatment and this severe decrease in the pore volume led to poor diffusion of reactants and products.

In contrast to conversion, the most important selectivity parameters (selectivity to cymenes, *p*-selectivity, and *iso/n*-propyl ratio) significantly differed for the materials with different structural properties. Selectivity to cymenes, the primary reaction (*o*- and *p*-cymenes) and isomerization (*m*-cymene) products, strongly depended on the dimensions and connectivity of the zeolite channels and decreased in the sequence of 1D > 2D > 3D (Fig. 6b). In the case of two aluminated AFI samples, selectivity to cymenes is rather constant and close to 100% within 184 min T-O-S indicating that cymenes are almost exclusively formed (Table 3). Relatively lower selectivity to cymenes for IPC-2, and Beta mainly caused by formation of *n*-propyl toluene (Tables 3 and 4) and secondary alkylation of primarily formed cymenes to other aromatic compounds, e.g. di-isopropyltoluene.

The isopropyl (cymene)/ *n*-propyl toluene ratio did not exceed 80 for MTW, IPC-2 and Beta zeolites in the course of the reaction during 184 min T-O-S (Fig. 6c). In contrast, for deGe-Al-AFI this ratio was found to be higher than 300 at the low T-O-S values and increased to > 550 at 184 min T-O-S. This is in line with the proposed mechanism of *n*-propyl toluene formation [40], evidencing the decisive role of 10-ring (10–12) channel intersections being able to accommodate the transition state of the bimolecular isomerization reactions between toluene and primarily formed cymene. Based on the results above, thus, the selectivity towards valuable branched products can be significantly increased over deGe-Al-AFI zeolites in comparison with conventional zeolites possessing either 1D (MTW) or multidimensional (IPC-2, Beta) pore system.

The selectivity to *p*-cymene over Beta and MTW was only 30% and 32%, respectively (Fig. 6d), which is lower than the values found for deGe-Al-AFI (41%), IPC-2 (43%) and Al-AFI (44%). Relatively low *para*-selectivity of Beta and MTW can be attributed to the higher B/L ratios or porosity for these zeolites. As a result, the kinetically favored *p*-cymene can be transformed to *o*- or *m*-cymene on the acid sites without steric limitation.

Therefore, the deGe-Al-AFI catalyst showed advantages to reach both relatively higher toluene conversion and commercially valuable *p*-cymene selectivity in the alkylation of toluene with isopropyl alcohol.

4. Conclusions

In the present work, new germanosilicate AFI zeolite with Si/Ge molar ratio equal to 8 was synthesized using 7, 11-dimethyl-6-azoniapropyl [5.6] undecane as SDA. This AFI zeolite was treated by one-step alumination or two-step degermanation/alumination and final products were investigated from the structure and acidity point of

views. The catalytic performance of these aluminated AFI zeolites was evaluated in alkylation of toluene with isopropyl alcohol. Incorporation of Al did not change the crystalline structure of the zeolite precursors, however, compared to two-step process, the pore-volume, BET area, and concentration and strength of acid sites were significantly lower for the zeolite obtained by one-step alumination. These results indicated that the degermanation step is necessary prior to the incorporation of aluminum due to the creation of hydroxyl nests by removal of germanium atoms from the framework.

The modification protocol of deGe-Al-AFI catalyst showed distinctive advantages in the alkylation of toluene with isopropyl alcohol to reach both relatively higher toluene conversion and selectivity to commercially valuable *p*-cymene due to the appropriate size of the zeolite channels and optimized B/L ratio. These factors cause more efficient formation of cymenes, especially *p*-cymene, by suppressing the secondary alkylation of cymenes and isomerization of *p*-cymene to *o*- or *m*-cymenes.

Acknowledgements

Authors thank to Dr. Valeria Kasnerik for measurement of SEM at J. Heyrovský Institute of Physical Chemistry. JC and MH acknowledge financial support of FV-17 by Bayerisch-Tschechische Hochschulagentur (BTHA). MO and MS thank Primus Research Program of the Charles University (project number PRIMUS/17/SCI/22 “Soluble zeolites”) and Neuron funding program (project number 31/2017).

References

- [1] J. Martínez-Triguero, M.J. Díaz-Cabanas, M.A. Cambor, V. Fornes, T.L. Maesen, A. Corma J. Catal. 182 (1999) 463–469.
- [2] J. Jiang, J. Yu, A. Corma, Angew. Chem. Int. Ed. 49 (2010) 3120–3145.
- [3] R. Bai, Q. Sun, N. Wang, Y. Zou, G. Guo, S. Iborra, A. Corma, J. Yu, Chem. Mater. 28 (2016) 6455–6458.
- [4] C.W. Jones, S.I. Zones, M.E. Davis, Appl. Catal. A Gen. 181 (1999) 289–303.
- [5] H. Kawagoe, K. Komura, J.-H. Kim, G. Seo, Y. Sugi, J. Mol. Catal. A Chem. 350 (2011) 1–8.
- [6] H.X. Zhang, A. Chokkalingam, P.V. Subramanian, S. Joseph, S. Takeuchi, M.D. Wei, A.M. Al-Enizi, H.-G. Jang, J.-H. Kim, G. Seo, K. Komura, Y. Sugi, A. Vinu, J. Mol. Catal. A Chem. 412 (2016) 117–124.
- [7] A. Ito, H. Maekawa, H. Kawagoe, K. Komura, Y. Kubota, Y. Sugi, Bull. Chem. Soc. Jpn. 80 (2007) 215–223.
- [8] E. Hu, Y.L.W. Huang, Q. Yan, D. Liu, Z. Lai, Microporous Mesoporous Mater. 126 (2009) 81–86.
- [9] <http://www.iza-structure.org/databases/>.
- [10] U.S. Patent (Ed.), Process for Preparing Molecular Sieves Using Adamantane Template, S.I. Zones, US, 1987.
- [11] S.I. Zones, Y. Nakagawa, Microporous Mesoporous Mater. 2 (1994) 543–555.
- [12] R.F. Lobo, M.E. Davis, Microporous Mesoporous Mater. 3 (1994) 61–69.
- [13] J. Přeč, D. Vitvarová, L. Lupinková, M. Kubš, J. Čejka, Microporous Mesoporous Mater. 212 (2015) 28–34.
- [14] H. Maekawa, Y. Kubota, Y. Sugi, Chem. Lett. 33 (2004) 1126–1127.
- [15] Y. Yun, M. Hernandez, W. Wan, X. Zou, J.L. Jorda, A. Cantin, F. Rey, A. Corma, Chem. Commun. 51 (2015) 7602–7605.
- [16] J.H. Kang, D. Xie, S.I. Zones, S. Smeets, L.B. McCusker, M.E. Davis, Chem. Mater. 28 (2016) 6250–6259.
- [17] A. Corma, M.J. Díaz-Cabanas, J.L. Jorda, C. Martínez, M. Moliner, Nature 443 (2006) 842–845.

- [18] J. Sun, C. Bonneau, A. Cantin, A. Corma, M.J. Díaz-Cabanac, M. Moliner, D. Zhang, M. Li, X. Zou, *Nature* 458 (2009) 1154–1157.
- [19] J. Jiang, Y. Xu, P. Cheng, Q. Sun, J. Yu, A. Corma, R. Xu, *Chem. Mater.* 23 (2011) 4709–4715.
- [20] F. Gao, Maguy Jaber, Krassimir Bozhilov, Aurelie Vicente, Christian Fernandez, V. Valtchev, *J. Am. Chem. Soc.* 45 (2009) 16580–16586.
- [21] M.V. Shamzhy, F. Elíasova, D. Vitvarova, M.V. Opanasenko, D.S. Firth, R.E. Morris, *Chem. Eur. J.* 22 (2016) 17377–17386.
- [22] X. Liu, H. Xu, L. Zhang, L. Han, J. Jiang, P. Oleynikov, L. Chen, P. Wu, *ACS Catal.* 6 (2016) 8420–8431.
- [23] M.V. Shamzhy, O.V. Shvets, M.V. Opanasenko, P.S. Yaremov, L.G. Sarkisyan, P. Chlubná, A. Zukal, V.R. Marthala, M. Hartmann, *J. Čejka, J. Mater. Chem.* 22 (2012) 15793.
- [24] M. Shamzhy, F.Sd.O. Ramos, *Catal. Today* 243 (2015) 76–84.
- [25] A. Rodríguez-Fernández, F.J. Llopis, C. Martínez, M. Moliner, A. Corma, *Microporous Mesoporous Mater.* 267 (2018) 35–42.
- [26] O.V. Shvets, N. Kasian, A.T. Zukal, J.I. Pinkas, J. Čejka, *Chem. Mater.* 22 (2010) 3482–3495.
- [27] C.A. Emeis, *J. Catal.* 141 (1993) 347–354.
- [28] A. Corma, V. Fornés, L. Forní, F. Márquez, J. Martínez-Triguero, D. Moscotti, *J. Catal.* 179 (1998) 451–458.
- [29] D.M. Roberge, H. Hausmann, W.F. Holderich, *Phys. Chem. Chem. Phys.* 4 (2002) 3128–3135.
- [30] M.V. Shamzhy, C. Ochoa-Hernández, V.I. Kasneryk, M.V. Opanasenko, M. Mazur, *Catal. Today* 277 (2016) 37–47.
- [31] S. Bordiga, C. Lamberti, F. Bonino, A. Travert, F. Thibault-Starzyk, *Chem. Soc. Rev.* 44 (2015) 7262–7341.
- [32] M.T. Portilla, F.J. Llopis, C. Martínez, S. Valencia, A. Corma, *Appl. Catal. A Gen.* 393 (2011) 257–268.
- [33] M. Osman, S. Al-Khattaf, U. Díaz, C. Martínez, A. Corma, *Catal. Sci. Technol.* 6 (2016) 3166–3181.
- [34] N. Žilková, P. Eliášová, S. Al-Khattaf, R.E. Morris, M. Mazur, J. Čejka, *Catal. Today* 277 (2016) 55–60.
- [35] C. Perego, P. Ingallina, *Green Chem.* 6 (2004) 274–279.
- [36] B. Wichterlová, J. Čejka, N. Žilková, *Microporous Mesoporous Mater.* 6 (1996) 405–414.
- [37] J. Čejka, G.A. Kapustin, B. Wichterlová, *Appl. Catal. A Gen.* 108 (1994) 187–204.
- [38] J. Čejka, A. Vondrová, B. Wichterlová, G. Vorbeck, R. Fricke, *Zeolites* 14 (1994) 147–153.
- [39] Z.R. Zhu, Q.L. Chen, W. Zhu, D.J. Kong, C. Li, *Catal. Today* 93 (2004) 321–325.
- [40] B. Wichterlová, J. Čejka, *J. Catal.* 146 (1994) 523–529.



Contents lists available at ScienceDirect

Catalysis Today

journal homepage: www.elsevier.com/locate/cattod

Synthesis of aggregation-resistant MFI nanoparticles

Hua Chen, Yong Zhou, Zdeněk Tošner, Jiří Čejka*, Maksym Opanasenko*

Department of Physical and Macromolecular Chemistry, Faculty of Science, Charles University, Hlavova 8, Prague 2, Czech Republic

ARTICLE INFO

Keywords:
MFI
Nanosized zeolite
Hybrid materials
Acylation
Quasi-homogeneous catalysis

ABSTRACT

Zeolites with particles of nm-scale size and restricted aggregation propensity were designed by decoration of zeolite surface with specific functional groups to address the problem of irreversible aggregation of respective nanoparticles. Highly crystalline MFI nano zeolites synthesized using hydrothermal method were functionalized with silanes of different nature (monodentate vs. polydentate, hydrophobic vs. hydrophilic) to investigate the influence of the type of surface functional groups on the stability of zeolite nanoparticles against aggregation in solution, accessibility of acid sites located in zeolite framework, and catalytic properties of resulting hybrid materials. The as-prepared materials were characterized by XRD, DLS, nitrogen adsorption, and adsorption of acetonitrile followed by FTIR, solid state ^{29}Si and ^{27}Al NMR, ICP-OES, TEM. Finally, we investigated the catalytic performance of designed materials in acylation of p-xylene to demonstrate that surface functionalization does not lead to deterioration of catalytic activity of the zeolite nanoparticles. Characterization data and catalytic results confirmed the improved stability of prepared nanoparticles with reasonable accessibility of acid sites. This finding can be used for preparation of aggregation-resistant zeolites dispersible in liquid-phase reaction mixtures in order to mimic homogeneous catalytic systems.

1. Introduction

Zeolites have been widely used in ion-exchange, gas adsorption and heterogeneous catalysis (e.g. in petrochemistry) [1–3], which is due to their unique structural features, such as pore size, channel dimensionality, and acidity [4,5]. Heterogeneous catalysis is essentially important in industrial chemistry because of easier separation of products, formation of a lower volume of waste substances and usually lower toxicity [6,7]. With the increasing demand for industrial chemicals and the pressure of the environmental issues, seeking for more effective, safe and environmentally friendly solutions, design and synthesis of novel catalysts, is highly desirable.

Utilization of zeolites as heterogeneous catalysts is restricted due to the limited size of the micropores (< 2 nm). The narrow pore openings and channels of conventional zeolites hinder the mass transport of bulky reactants [8,9]. To overcome this limitation, an effective way is to prepare zeolites possessing extra-large pores (> 8.0 Å) [10–14]. However, most of extra-large pore zeolites are germanosilicates. The high cost, low thermal and chemical stability restrict their applications. On the other hand, great efforts also have been undertaken to introduce meso- or macro porosity into zeolites to design hierarchical zeolites [15–18]. The synthetic strategies toward hierarchical zeolites include “top-down” and “bottom-up” methods, which involve partial removal

of framework atoms (Si, or Al) by acid or basic solution treatments [19–21], or using of soft (surfactants, polymers), hard (carbon nanostructures) templates as porogens [22,23]. However, the top-down approach can result in decreasing crystallinity and lowering thermal and chemical stability of resulting materials. On the other hand, producing hierarchical zeolites with templates will increase the cost, and uncontrollable mesopore size limits their large-scale application of respective materials as well [26].

Alternatively, a straightforward solution to overcome diffusion limitation in zeolite catalysts is to decrease the crystal size [24,25]. Compared with the micron-sized counterparts, the decrease in the zeolite crystal size to nanometer scale can endow zeolites with outstanding characteristics, such as the short diffusion path and large external surface area, which can well overcome the bulky reagents mass transport limitation [26,27]. These characteristics not only provide new possibilities for traditional applications in heterogeneous catalysis and molecular separation processes, but also lead to the expansion of their use to other emerging fields, such as chemical sensing, optical devices, biomedical and biological analyses [28]. However, nanosized zeolites suffer from aggregation because of high specific surface energy, which restricts their utilization [29]. The aggregation of zeolite nanoparticles can be prevented by adding emulsifying agents like detergents or surfactants [30]. Functionalization or coating of silica and zeolite

* Corresponding author.

E-mail address: jiri.cejka@jh-inst.cas.cz (J. Čejka).

<https://doi.org/10.1016/j.cattod.2019.10.026>

Received 18 February 2019; Received in revised form 9 September 2019; Accepted 15 October 2019
0920-5861/ © 2019 Elsevier B.V. All rights reserved.

Please cite this article as: Hua Chen, et al., Catalysis Today, <https://doi.org/10.1016/j.cattod.2019.10.026>

nanoparticles surface with organosilane reagents to reduce the aggregation has been reported as well [31,32]. However, only additional mesopores are formed by close packing of nanoparticles upon calcination [32]. Therefore, the obtained materials were not real aggregation-resistant catalysts, which significantly limit the utilization of such materials as reusable catalysts with predictable surface properties and activity. Resasco and other researchers did a lot of attempts to functionalize the surface of zeolite crystals with organosilanes and tune the hydrophobic properties of zeolites [33,34]. Their works inspired us to design and synthesis of aggregation-resistant zeolite catalyst by careful silylation of nanosized zeolite crystals.

In this work, we have developed a new strategy for the synthesis of aggregation-resistant zeolite by silylation of the MFI nanocrystals. Four organosilanes with different size and nature were tested. Compared to the conventional zeolites with bulk crystals and non-functionalized nm-size zeolites, the resulting hybrid materials showed significantly less aggregation under both static (for 10 days) and catalytic (acylation of p-xylene with butyryl chloride) conditions, which suggested that they can be considered as good candidates for pseudo-homogeneous catalytic systems.

2. Experimental

2.1. Materials

For synthesis of MFI type nanosized zeolite, tetraethylorthosilicate (TEOS, 98%), tetrapropylammonium hydroxide solution (TPAOH, 40 wt %), sodium aluminate (NaAlO_2), and L-lysine ($\text{C}_6\text{H}_{14}\text{N}_2\text{O}_2$, 98%), ethoxydimethylphenylsilane (98%), triethoxyphenylsilane (98%), (4-biphenyl)triethoxysilane (98%) and 3-(ethoxydimethylsilyl)propylamine (98%), acetone (99%) were supplied by Sigma Reagent Company. Sodium hydroxide (NaOH , 98%) was purchased from VWR Reagent Company, p-xylene (99.5%), butyryl chloride (99%), dodecane (99%) were supplied by Sigma-Aldrich.

2.2. Preparation of catalysts

2.2.1. Synthesis of nanosized MFI zeolites

The molar compositions of the mixture was 1.0 SiO_2 /0.45 TPAOH/0.003 Al_2O_3 /0.015 Na_2O /0.1L-lysine/9 H_2O . The synthesis procedure followed the Zhang's experiment [35]. Typically, TEOS was mixed with TPAOH and deionized water at room temperature with fast stirring until completely hydrolyzed, followed by the addition of NaAlO_2 to the reaction mixture with fast stirring for another 30 min. Then L-lysine was added to the uniform solution. The gel mixture was continuously stirred to evaporate the excess water to get required water-to-silica ratio and then transferred into a Teflon-lined stainless steel autoclave for crystallization. The crystallization was conducted in a conventional oven initially at 80 °C for 2 days and subsequently at 170 °C for 1 day under static conditions. The as-synthesized solid products were centrifuged, washed with water several times, and then dried at 80 °C in the oven overnight, followed by calcination at 550 °C for 6 h.

2.2.2. Ion-exchange

Aqueous 1 M NH_4NO_3 solution was used (1 g zeolites with 30 mL solution) with fast stirring in 80 °C for 2 h. Ion exchange procedure was repeated 3 times. After filtration, sample was dried at 80 °C in the oven followed by calcination at 550 °C for 4 h. Obtained sample was denoted as N-MFI [36].

2.2.3. Functionalization of N-MFI

Firstly, 50 mg of N-MFI was added to 10 mL of acetone. Further, the solution was sonicated to form a suspension. After addition of required silane (0.04 mol/g), reaction mixture was sonicated 3 times 10 min. per time in an ice bath. Then centrifuge the solution and washed the solid products with acetone 3 times. The final solid products were dried at

80 °C. The N-MFI functionalized by triethoxyphenylsilane and ethoxydimethylphenylsilane were denoted as N-MFI-S1 and N-MFI-S2, respectively.

2.3. Characterization

The structure and crystallinity of nanozeolites were assessed using Bruker AXS D8 Advance diffractometer with $\text{Cu K}\alpha$ radiation ($\lambda = 0.154 \text{ nm}$) in the 2θ range of 5–50° at a scanning rate of 4°/min

The elemental analysis was carried out using Thermo Scientific ICAP 7000 inductive coupled plasma-optical emission spectroscopy (ICP-OES). Prior to the measurement, samples were mineralized in a mixture of concentrated hydrochloric, nitric and hydrofluoric acid.

The nitrogen adsorption and desorption measurements were carried out at –196 °C using the Micromeritics GEMINI II 2370 volumetric Surface Area Analyzer. Before the sorption measurements, all samples were degassed at 150 °C in a Micromeritics FlowPrep 060 instrument, (heating rate 10 °C/min) for 4 h. The surface area was evaluated using BET method. The t-plot method was applied to determine the volume of micropores. The adsorbed amount at relative pressure $p/p_0 = 0.98$ reflects the total adsorption capacity. The pore size distributions were calculated using the BJH model from the desorption branch of the isotherms.

The concentration and type of acid sites were determined by adsorption of acetonitrile as a probe molecule followed by FTIR spectroscopy (Nicolet iS50 FT-IR) using the self-supported wafer technique. Prior to adsorption of the probe molecule, the wafers of zeolite samples were activated by overnight evacuation at temperature 250 °C.

High-resolution transmission electron microscopy (HRTEM) were carried out on a JEOL JEM-2011 electron microscope operating at an accelerating voltage of 200 kV. The HRTEM images were recorded using a 9 Gatan 794 CCD camera.

Dynamic light scattering (DLS) was used to identify particles size distribution. Prior the measurement, 10 mg of zeolite was introduced in 10 mL of the acetone and mixture was sonicated for 10 min.

Solid-state ^{27}Al and ^{29}Si NMR spectra were obtained using a Bruker Avance III HD spectrometer working with a 9.4 T standard-bore superconducting magnet (27Al Larmor frequency of 104.26 MHz). The samples were packed into a thin-wall 3.2 mm zirconia rotor, and rotated at a MAS rate of 15 kHz using a Bruker 3.2 mm HX CP-MAS probe. A pulse of 1.0 μs (B1 field approx. 95 kHz) with a relaxation delay of 1 s was applied and 2048 transients were averaged. The spectra were referenced to saturated solution of $\text{Al}(\text{NO}_3)_3$ in D_2O . ^{29}Si spectra (79.49 MHz) were acquired employing the pulse length of 2.0 μs (B1 field approx. 63 kHz) and repetition time of 15 s. For referencing, tetramethylsilane solution was used. The spectra were averaged over 512 or 4096 transients, depending on the sample. In all cases, no proton decoupling was applied.

2.4. Aggregation test

Catalyst was dispersed in acetone (1 g/L), under sonication in ice bath for 10 min (3 sonication cycles). Then, 1 mL of the homogeneous solution was taken to evaluate the particle size by DLS.

2.5. Catalytic test

The catalytic test was performed in the liquid phase at 130 °C and at atmospheric pressure in a multi-experiment workstation StarFish. Prior to reaction, the catalysts were activated at 150 °C for 90 min with the rate of 10 °C/min. In all cases, 50 mg of catalyst powder, p-xylene (5 mL, 40 mmol), butyryl chloride (5 mmol) and 0.5 g of dodecane (internal standard) were added to the two-necked flask equipped with a condenser and a thermometer. The samples of the reaction mixture were taken periodically and analyzed using Agilent 6850 GC equipped a polar DB-WAX column (length 20 m, diameter 0.180 mm, and film

thickness 0.3 μm) and flame ionization detector.

Turnover frequency was calculated based on following formula:

$$\text{TOF} = \frac{N * \text{Con.}}{(CL + CB) * M * t}$$

Where N stands for 5 mmol of butyryl chloride, Con. is the conversion after reaction time t , $(CL + CB)$ is the concentration of acid sites based on acetonitrile adsorption followed by FTIR and M is the weight of the catalyst (50 mg).

3. Results and discussion

In order to optimize the aggregation properties of nanosized zeolite particles four types of silanes were chosen:

- tridentate (able to form three bonds per one molecule) small-(containing phenyl group) and large-size (with biphenyl group) silanes were selected to investigate the influence of π - π interaction between aromatic groups and size of these groups on the degree of nanoparticles aggregation;
- material synthesized using monodentate silane (ethoxydimethylphenylsilane) was compared with that prepared using triethoxyphenylsilane to confirm the necessity to limit the cross-linking capacity of the functionalizing agent;
- silane containing relatively hydrophilic amino-group was chosen for comparison with silanes containing exclusively alkyl- and aryl-groups and providing high hydrophobicity of the resulting nanoparticles.

Proposed concept is chemically very simple (Scheme 1) and related to the well-known modification of silanols on the surface of zeolite crystals with organic groups using organosilanes [37,38].

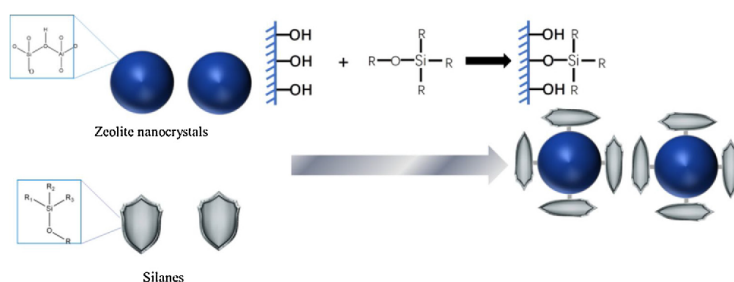
Dynamic light scattering (DLS) was applied to investigate the particle size distribution of the zeolite samples obtained. The DLS data demonstrated that functionalization of the zeolite particles did not change significantly average size (Fig. 1. black curves), which slightly increased from about 65 nm for N-MFI to 70–95 nm for the modified species. For evaluation of aggregation behavior of both purely zeolitic and functionalized nanoparticles, the particle size change after 10 days static state (Fig. 1. red curves) was chosen as the criterion. From the DLS results, the average size of non-functionalized N-MFI crystals increased almost 5 times (398% increase, Fig. 1A) after 10 days that indicate severe aggregation of the nanoparticles due to the high surface free energy. TEM of N-MFI after 10 days provided additional evidence of the aggregation of nanocrystals, which shown in Fig. 5A. The N-MFI functionalized with ethoxydimethylphenylsilane showed remarkable aggregation resistance with almost no shift of the maximum on DLS curve and only minor increase in the average particle size (37%) caused by the formation of the particles of > 100 nm size (shoulder on the red plot, Fig. 1C), the TEM image of N-MFI-S2 again showed the discrete MFI nanoparticles uniformly dispersed in acetone after 10 days (Fig. 5B). This result can be explained by the optimum hydrophobicity

of the dimethylphenylsilyl groups allowing to avoid the aggregation of the nanoparticles under conditions used as well as the inability of initial silane to form more than one covalent bond with silanol groups that provide the absence of interparticle linkages. In contrast, when N-MFI was functionalized with tridentate triethoxyphenylsilane and especially (4-biphenyl)triethoxysilane, the aggregation behavior was just slightly better (215% average particle size increase after 10 days, Fig. 1B) or comparable (397% increase, Fig. 1D) to the non-modified sample. In the latter case, the aggregation resistance was the worst despite the largest size of substituent among the tested silanes, this is probably caused by π - π interaction of biphenyl rings with each other facilitating interparticle conjugation more efficiently in compared with phenyl counter silane. When more hydrophilic functionalization agent (e.g. amino-containing) was used, even low denticity of initial silane does not provide sufficient stability of the resulting nanoparticles in the solution (207% average particle size increase after 10 days, Fig. 1E). Difference in the concentration or distribution of functional groups over the surface of zeolite particles caused by the differences in the properties of used silanes (hydrophilicity, presence of aromatic rings, possibility to form intermolecular H-bonds) can be additional factor for the distinction in the properties of functionalized samples. Based on the DLS results, N-MFI functionalized by phenylsilyl- (N-MFI-S1, reference sample) and dimethylphenylsilyl-groups (N-MFI-S2, sample most stable against aggregation) was chosen for further study and comparison with N-MFI.

TG analysis was carried out in order to assess the amount of organosilanes attached to the zeolite nanocrystals (see Fig. 2). The total weight loss in the tested samples are 5.48% and 4.90% for N-MFI-S1 and N-MFI-S2 respectively, which suggested the amount of two silanes attached during the silylation treatment was comparable. The TG results confirmed the better stability of N-MFI-S2 was mainly attributed to the monodentate property of ethoxydimethylphenylsilane instead of the amount of silane capped on the nanoparticles.

The preservation of zeolite structure and crystallinity of the synthesized materials was evaluated by X-ray powder diffraction. Fig. 3. shows the diffraction patterns of N-MFI, N-MFI-S1 and N-MFI-S2. Sharp diffraction peaks at 7.6° , 8.5° , 23° , 23.9° and 24.4° of 2θ , which are the typical characteristic diffraction peaks of MFI zeolite [35], were observed in the N-MFI sample. This result confirms the MFI structure and high crystallinity of this as-synthesized sample. After the functionalization, the structure of zeolites did not change (both peak positions and intensities in XRD patterns were the same when compared with N-MFI, Fig. 3), which means that the introduction of organic functional groups did not influence the structure of zeolites.

The TEM images were in agreement with the DLS and XRD data of the samples studied (Fig. 4). Observed nanoparticles are uniform and of similar size in the range 60–70 nm for N-MFI, N-MFI-S1 and N-MFI-S2 samples. Average particle sizes are slightly lower in comparison with those estimated using DLS. The reason is that in the latter case the existence of even small fraction of aggregated particles with the



Scheme 1. Concept of approach for the synthesis of aggregation-resistant zeolites using silane as aggregation prohibit.

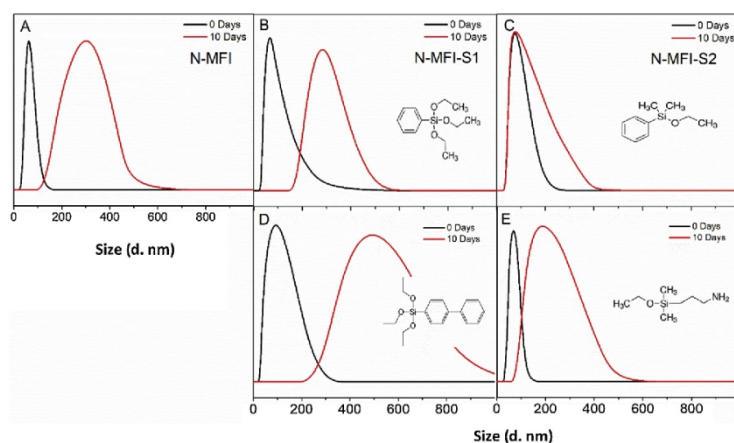


Fig. 1. DLS curves of the as-synthesized nanosized MFI and different silanes modified samples after 10 days static state: (A) non-functionalized N-MFI, (B) triethoxyphenylsilane (N-MFI-S1), (C) ethoxydimethylphenylsilane (N-MFI-S2), (D) (4-biphenyl)triethoxysilane, (E) 3-(ethoxydimethylsilyl)propylamine.

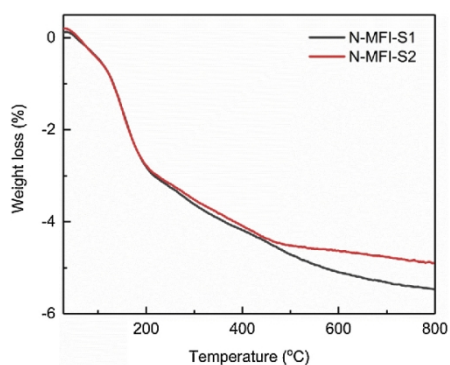


Fig. 2. TG analyses of N-MFI-S1 and N-MFI-S2.

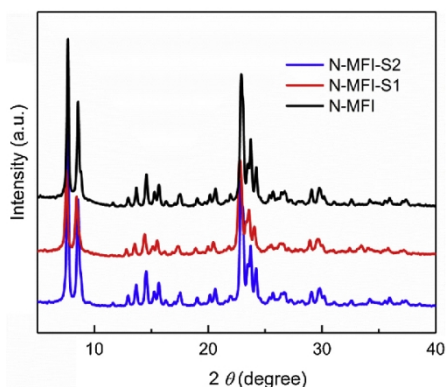


Fig. 3. XRD of N-MFI, N-MFI-S1 and N-MFI-S2.

size > 100 nm, which were not spotted on TEM images, resulting in the shift of the median of the size distribution. From TEM images on Fig. 4, modification of the surface of MFI nanoparticles with substituted silanes practically does not affect the size, morphology and crystallinity of functionalized nano zeolites. HRTEM images (Fig. 4B, D, F) revealed that all samples have good crystallinity and microporosity. The results of HRTEM indicated that the lattice spacing around 1.3 nm was associated to the (001) lattice plane of the MFI type zeolite, which corresponds to the literature data [39].

Blocking of the pore entrances by functionalization agent can proceed during surface modification of porous materials resulting in deterioration of textural properties of the final material. Therefore, adsorption characteristics of all functionalized samples were examined using nitrogen as probe molecule and compared with N-MFI (Fig. S-1 and Table 1). All the isotherms exhibit the same type (I + IV) and similar shape (Fig. S-1). A sharp uptake at $p/p_0 > 0.8$ corresponds to the adsorption in the interparticle voids of the mesopore scale. The same values of the micropore volume for N-MFI ($V_{\text{micro}} = 0.106 \text{ cm}^3/\text{g}$) and functionalized samples ($V_{\text{micro}} = 0.103 - 0.104 \text{ cm}^3/\text{g}$) evidences the absence of pore blocking phenomena under conditions used. At the same time, BET area decreased (Table 1) after functionalization due to the condensation of silanes with silanols on the external surface. The drop in S_{BET} value (69–76 m^2/g) roughly corresponds to the decrease in S_{ext} (65–74 m^2/g). However, the porosity of N-MFI, N-MFI-S1 and N-MFI-S2 after activation at the relatively high temperature (250 °C) dramatically changed (Fig. S-2). For non-functionalized samples, aggregation at 250 °C resulted in a decrease in the external surface area accompanied by increase in the micropore volume due to the collapse of interparticle mesoporous system. In the case of functionalized materials, the apparent decrease in the BET area (from > 300 to about 60 m^2/g) and micropore volume (from 0.1 to < 0.005 cm^3/g) was observed. This is probably caused by the degradation of organic groups due to the high-temperature pre-treatment causing the coking and plugging of the channel in the samples (Table S-1). Utilization of the interparticle voids limited by external surface of zeolite nanoparticles as the reaction space for anchoring of functional groups lead also to the decrease of total pore volume (Table 1).

For N-MFI sample, the Si/Al ratio obtained by ICP/OES (Table 1) was slightly lower in comparison with the Si/Al ratio used for the synthesis (133 and 167, respectively). Functionalization using silylation agents naturally resulted in the increase in the silicon atoms fraction and thus increases in Si/Al ratio up to 174 (Table 1).

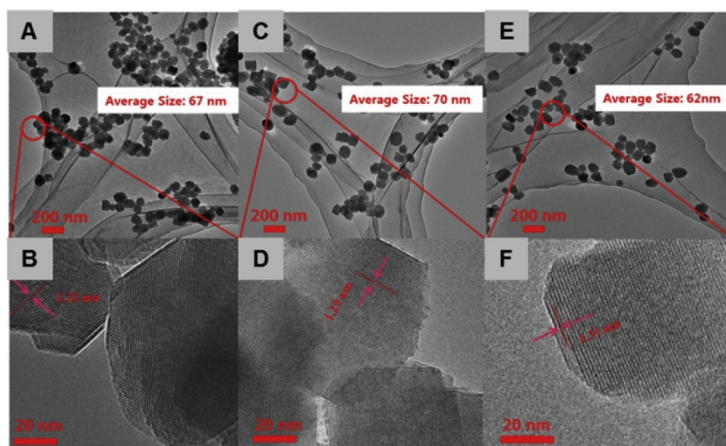


Fig. 4. TEM images of N-MFI (A, B), N-MFI-S1(C, D) and N-MFI-S2 (E, F).

In typical IR spectra of functionalized samples (Fig. S-3), the bands related C–H stretching (2982, 2943, 2884 cm^{-1}) and bending (1478/1460, 1385 cm^{-1}) vibrations can be found [40]. The band at around 3745 cm^{-1} corresponds to the terminal OH groups bound to silicon framework atoms. Intensity of this line was significantly reduced in

comparison with that of the parent N-MFI sample due to the consumption of the fraction of surface silanol groups for condensation with functionalized silanes. The number of Brønsted sites and Lewis sites determined using acetonitrile as probe molecule were 50 and 10 $\mu\text{mol/g}$ for N-MFI, while totaled 10 and 10 $\mu\text{mol/g}$ for N-MFI-S2, 30

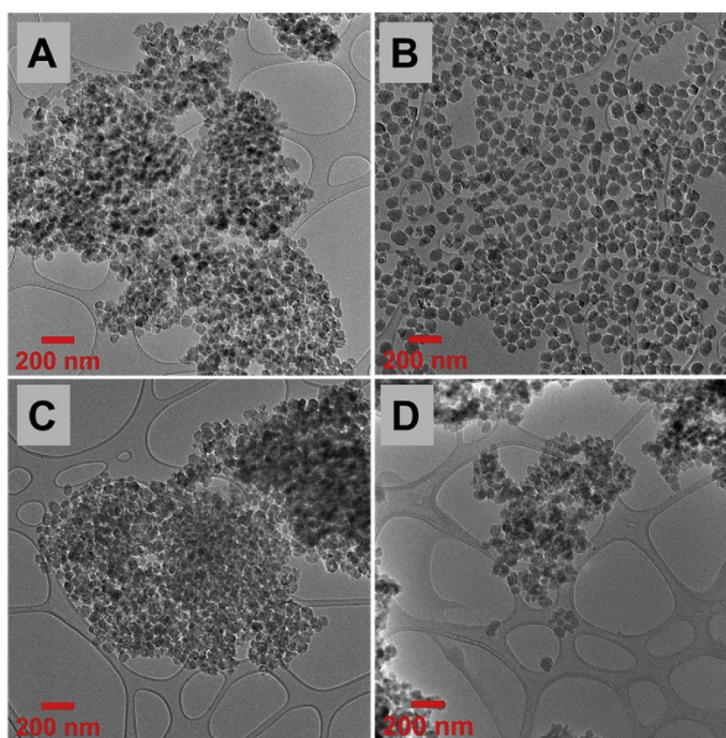


Fig. 5. TEM images of N-MFI (A, C) and N-MFI-S2 (B, D) dispersed in acetone for 10 days (A, B) or after catalytic reaction (C, D).

Table 1
Chemical composition and textural properties of N-MFI, N-MFI-S1, N-MFI-S2 and commercial MFI.

	Si/Al ^a	S _{BET} (m ² /g) ^b	S _{ext} (m ² /g)	V _{micro} (cm ³ /g) ^c	V _{total} (cm ³ /g)
N-MFI	133	378	178	0.106	0.454
N-MFI-S1	174	309	113	0.103	0.372
N-MFI-S2	151	302	104	0.104	0.331
C-MFI [40]	140	378	n.d.	0.192	n.d.

^a Measured by ICP/OES. ^b Specific surface area (BET) given by N₂ adsorption at -196 °C. ^c Calculated by t-plot method. n.d.: not determined.

and 10 μmol/g for commercial MFI, respectively. In the case of N-MFI-S1, concentration of acidic sites was below the FTIR detection limit. We assumed two main reasons for the lower (for N-MFI-S2) or even negligible (for N-MFI-S1) concentration of acid sites determined by FTIR in comparison with parent N-MFI: 1) the change of the Al state during functionalization treatment either because of partial breaking of Si-O-Al bonds or due to the interaction of Al with silylating agent; 2) degradation of organic part of functionalized samples due to the high-temperature pre-treatment (required for evacuation of adsorbed molecules prior the IR measurement) resulting in the lower accessibility of acid sites by probe molecules in the following experiment.

To check the first assumption, we performed ²⁷Al and ²⁹Si MAS-NMR spectroscopy measurements for the samples before and after functionalization (Fig. 6). The line located at 56 ppm in ²⁷Al MAS-NMR spectra is assigned to framework tetrahedral Al atoms [42]. No other peaks (e.g. related to the extra-framework octahedral aluminum) were detected for both the initial and modified zeolites (Fig. 6A) evidencing the maintenance of Al positions upon functionalization, and exclusively framework location of aluminum atoms for all the samples studied. In contrast, the surrounding of Si atoms was substantially changed after anchoring organosilanes to the surface of zeolite nanoparticles (Fig. 6B). Two dominating resonance peaks in the ²⁹Si-MAS NMR spectra of N-MFI were observed. The signal at -114 ppm can be assigned to Si^δ(OSi)₄ sites (Q4) in the framework, while broad resonance peak around -109 ppm is typically ascribed to HOSi^δ(OSi)₃ sites (Q3) [43]. The dramatic decrease in the intensity of Q3 peak occurred in the spectra of N-MFI-S1 and N-MFI-S2 samples that indicates the complete condensation of surface silanol groups with alkoxy-silyl groups of silanes. As a result, both ²⁷Al and ²⁹Si NMR spectra of functionalized materials contain the single peak of Q4 evidencing the uniformity of the

atoms in the frameworks.

The catalytic activity of N-MFI-S2 was evaluated in acylation of p-xylene with butyryl chloride (Fig. 7). Since the reaction under study can proceed over both Brønsted and Lewis acid sites, the evaluation of the catalyst activity (turnover frequency values, TOF) was done using the total concentration of active sites. The commercial MFI (Si/Al = 140, designated as C-MFI) with chemical composition similar to the samples under investigation was selected for comparison. C-MFI has clearly discrete spherical morphology with mean diameter of particles about 2 μm (see Fig. S-4). The results of catalytic test indicate that C-MFI reached the highest butyryl chloride conversion (Fig. 7A) because it contains more acid sites (60 μmol/g), while in terms of TOF (Fig. 7B), N-MFI-S2 exhibited the highest activity (TOF = 602 h⁻¹). The non-functionalized N-MFI (TOF = 173 h⁻¹) did not surpass the efficiency of commercial sample (TOF = 390 h⁻¹). Taking into account the aggregation stability of the samples used (see discussion above), the agglomeration of the nanoparticles is the most probable explanation of relatively low activity of the N-MFI material. The results of DLS for N-MFI sample recovered after full catalytic run (Fig. S-5) showed the increase of the average particle size from 65 to 210. TEM images (see Fig. 5C) of used N-MFI showed severe aggregation of nanocrystals, larger clusters of nanoparticles had size around 1 μm, which confirms the assumption made. N-MFI-S2 sample also suffers from aggregation under relatively severe conditions of activation and reaction resulting in the particle size increase (Fig. 5D and Fig. S-5), however, this increase was moderate in comparison with non-functionalized zeolite evidencing the advantage of modified catalysts in terms of both activity and stability.

4. Conclusions

We have demonstrated a new method to prepare aggregation-resistant MFI zeolites with nm-scale size around 70 nm. Among the tested silanes with different nature and size, ethoxydimethylphenylsilane was found to be the best reagent to functionalize the nanosized zeolites. The ethoxydimethylphenylsilane-silylated sample (N-MFI-S2) almost preserved their crystal size both in dispersion in acetone for 10 days and after catalytic test in acylation of p-xylene under harsh reaction conditions, which exhibited obviously improved aggregation-resistant performances. Together with the relatively better catalytic activity, this proof of concept work showed the design and preparation of aggregation-resistant zeolites dispersible in liquid-phase reaction mixtures, and this kind of catalyst could be potentially used in quasi-homogeneous

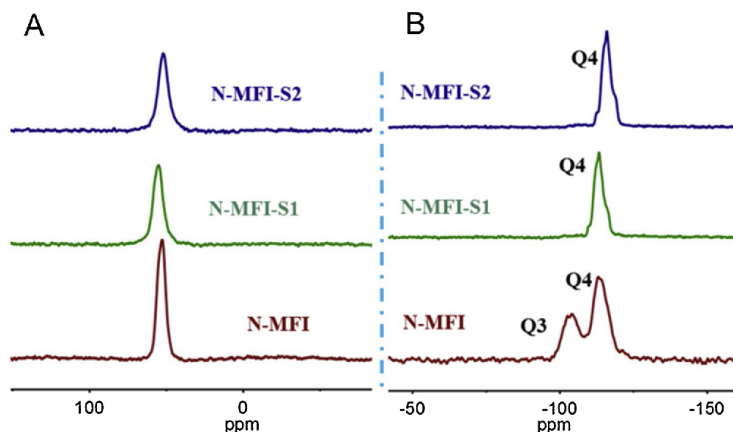


Fig. 6. (A) ²⁷Al and (B) ²⁹Si MAS NMR spectra of N-MFI, N-MFI-S1 and N-MFI-S2.

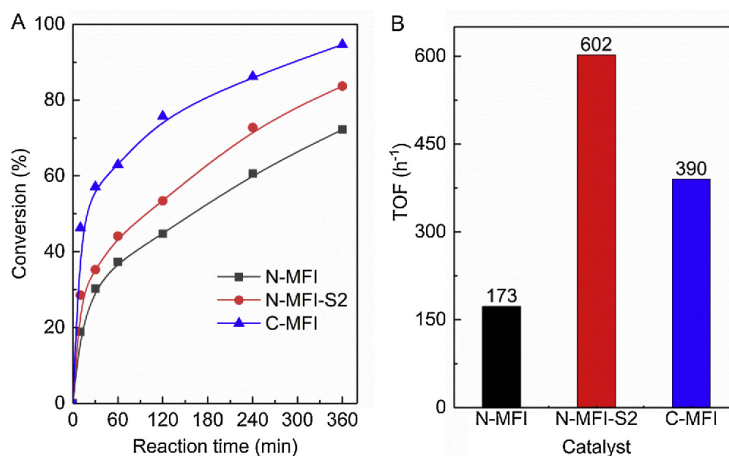


Fig. 7. (A) Conversion of butyryl chloride with reaction time and (B) TOF over N-MFI, N-MFI-S2 and C-MFI catalysts in acylation of p-xylene. Conditions: 5 ml p-xylene, 5 mmol butyryl chloride, 0.5 g dodecane (internal standard), 130 °C.

catalytic systems.

Acknowledgements

The authors thank following people for the assistance with characterization of the samples: Dr. Miroslav Štěpánek (DLS), Dr. Mariya Shamzhy (FTIR), Dr. Michal Mazur (TEM) and Dr. Jana Havlíčková (TG), Dr. Ondřej Vaněk (Centrifuge).

MO thanks Primus Research Program of the Charles University (project number PRIMUS/17/SCI/22 “Soluble zeolites”) and Neuron funding program (project number 31/2017). JČ acknowledges the Czech Science Foundation for the support of the project EXPRO (19-27551X).

References

- [1] J. Prech, P. Pizarro, D.P. Serrano, J. Cejka Chem. Soc. Rev. 47 (2018) 8263–8306.
- [2] D.P. Serrano, J.A. Melero, G. Morales, J. Iglesias, P. Pizarro Catal. Rev.: Sci. Eng. 60 (2018) 1–70.
- [3] M. Shamzhy, M. Opanasenko, P. Concepcion, A. Martinez Chem. Soc. Rev. 48 (2019) 1095–1145.
- [4] M. Moliner, T. Willhammar, W. Wan, J. Gonzalez, F. Rey, J.L. Jorda, X. Zou, A. Corma, J. Am. Chem. Soc. 134 (2012) 6473–6478.
- [5] W. Schwieger, A.G. Machoke, T. Weissenberger, A. Inayat, T. Selvam, M. Klumpp, A. Inayat, Chem. Soc. Rev. 45 (2016) 3353–3376.
- [6] A. Galadima, O. Muraza, J. Ind. Eng. Chem. 31 (2015) 1–14.
- [7] B.M. Weckhuysen, J. Yu, Chem. Soc. Rev. 44 (2015) 7022–7024.
- [8] W.J. Roth, P. Nachtigall, R.E. Morris, J. Cejka Chem. Rev. 114 (2014) 4807–4837.
- [9] M. Opanasenko, M. Shamzhy, F. Yu, W. Zhou, R.E. Morris, J. Cejka Chem. Sci. 7 (2016) 3589–3601.
- [10] B. Yang, J. Jiang, H. Xu, H. Wu, M. He, P. Wu Angew. Chem. 130 (2018) 659–9663.
- [11] M. Hartmann, W. Schwieger Chem. Soc. Rev. 45 (2016) 3311–3322.
- [12] B. Chen, M. Eddaoudi, S.T. Hyde, M. O’Keeffe, O.M. Yaghi Science 291 (2001) 1021–1023.
- [13] J.L. Paillaud, B. Harbuzari, J. Patarin, N. Bats Science 304 (2004) 990–992.
- [14] J. Jiang, J.L. Jorda, M.J. Diaz-Cabanas, J. Yu, A. Corma Angew. Chem. Int. Ed 49 (2010) 4986–4988.
- [15] J. Ramirez, C.H. Christensen, K. Egeblad, C.H. Christensen, J.C. Groen Chem. Soc. Rev. 37 (2008) 2530–2542.
- [16] D.P. Serrano, J. Aguado, J.M. Escola, J.M. Rodriguez, A. Peral Chem. Mater. 18 (2006) 2462–2464.
- [17] D.P. Serrano, J.M. Escola, P. Pizarro Chem. Soc. Rev. 42 (2013) 4004–4035.
- [18] K. Li, J. Valla, J. Martinez ChemCatChem 6 (2014) 46–66.
- [19] J. Perez-Ramirez, C.H. Christensen, K. Egeblad, C.H. Christensen, J.C. Groen, Chem. Soc. Rev. 37 (2008) 2530–2542.
- [20] M. Opanasenko, W. Parker Jr, M. Shamzhy, E. Montanari, M. Bellettato, M. Mazur, R. Millini, J. Cejka, J. Am. Chem. Soc. 136 (2014) 2511–2519.
- [21] H. Hernandez, I. Moreno, J. Feroso, C. Ochoa-Hernandez, P. Pizarro, J.M. Coronado, J. Cejka, D.P. Serrano, Biomass Convers. Bior 7 (2017) 289–304.
- [22] K. Zhu, K. Egeblad, C.H. Christensen, Eur. J. Inorg. Chem. 2007 (2007) 3955–3960.
- [23] Z.P. Wang, C. Li, H.J. Cho, S.C. Kung, M.A. Snyder, W. Fan, Direct J. Mater. Chem. A 3 (2015) 1298–1305.
- [24] G.H. Yang, X.F. Zhang, S.Q. Liu, K.L. Yeung, J.Q. Wang, J. Phys. Chem. Solids 68 (2007) 26–31.
- [25] G. Reding, T. Maurer, B. Czarnetzki, Microporous Mesoporous Mater. 57 (2003) 83–92.
- [26] F. Mohammadparast, R. Halladj, S. Askari, Chem. Engin. Commun. 202 (2015) 542–556.
- [27] S.M. Alipour, Chin. J. Catal. 37 (2016) 671–680.
- [28] S. Mintova, M. Jaber, V. Valtchev, Chem. Soc. Rev. 44 (2015) 7207–7233.
- [29] V.S. Raghuwanshi, U.M. Garusinghe, J. Ilavsky, W.J. Batchelor, G. Garnier, J. Colloid Interface Sci. 510 (2018) 190–198.
- [30] X. Su, R. Kanjanawarut, ACS Nano 3 (2009) 2751–2759.
- [31] R.P. Bagwe, L.R. Hilliard, W. Tan, Langmuir 22 (2006) 4357–4362.
- [32] D.P. Serrano, J. Aguado, G. Morales, J.M. Rodriguez, A. Peral, M. Thommes, J.D. Epping, B.F. Chmelka, Chem. Mater. 21 (2009) 641–654.
- [33] P.A. Zapata, J. Faria, M.P. Ruiz, R.E. Jentoft, D.E. Resasco, J. Am. Chem. Soc. 134 (2012) 8570–8578.
- [34] K. Chen, J. Kelsey, J.L. White, L. Zhang, D. Resasco, ACS Catal. 5 (2015) 7480–7487.
- [35] Q. Zhang, G.R. Chen, Y.Y. Wang, M.Y. Chen, G.Q. Guo, J. Shi, J. Luo, J.H. Yu, Chem. Mater. 30 (2018) 2750–2758.
- [36] G.L. Wang, W. Wu, W. Zan, X.F. Bai, W.J. Wang, X. Qi, O.V. Kikhtyanin, Trans. Nonferrous Met. Soc. China 25 (2015) 1580–1586.
- [37] Y.P. Guo, H.J. Wang, Y.J. Guo, L.H. Guo, L.F. Chu, C.X. Guo, Chem. Eng. J. 166 (2011) 391–400.
- [38] P.A. Zapata, Y. Huang, M.A. Borja, D.E. Resasco, J. Catal. 308 (2013) 82–97.
- [39] N. Wang, W. Qian, K. Shen, C. Su, F. Wei, Chem. Commun. (Camb.) 52 (2016) 2011–2014.
- [40] K. Zhang, R.P. Lively, J.D. Noel, M.E. Dose, B.A. McCool, R.R. Chance, W.J. Koros, Langmuir 28 (2012) 8664–8673.
- [42] A.W.S. Guarino, R.A.S. San Gil, H. Polivanov, S.M.C. Menezes, J. Braz. Chem. Soc. 8 (1997) 581–586.
- [43] W. Song, R.E. Justice, C.A. Jones, V.H. Grassian, S.C. Larsen, Langmuir 20 (2004) 8301–8306.

Curriculum Vitae

Personal details

Fullname : Yong Zhou (周 勇)
Date of Birth : June 26th, 1989
Place of Birth : Xiangtan, China
Gender : Male
Cell Phone : (+420) 775543246
Email : zhouyo@natur.cuni.cz

Education degree

2016–now

Ph.D. studying at Charles University in Prague,

Physical Chemistry

Thesis topic: Design and catalytic applications of novel nanostructured materials

Supervisor: Dr. Maksym Opanasenko. Advisor: Prof. Jiri Čejka.

2013–2016

Master degree at Xiangtan University,

Materials Science and Engineering

Diploma thesis: Surface tension and Raman spectrometric of alkali halide solutions

Supervisor: Prof. Chang Q. Sun.

2009-2013

Bachelor degree at Hunan University of Arts and Science

Physics

Experience

Zeolites synthesis, functionalization and catalysis. Hydrogen bond asymmetric coupling relaxation analysis resolving abnormal properties of water and ice. Skills in operation for materials characterizations and testing: XRD, N₂ adsorption, FTIR, Raman spectroscopy, DLS, NMR and catalytic tests at Starfisher.

Publications

15 publications including 1 patent.

In addition, one manuscript is in preparation.

1. Zhang, W.D.¹, **Zhou, Y.**¹, Shamzhy, M., Molitorisová, S., Opanasenko, M., Giroir-Fendlera, A., Toward rational design of Co₃O₄ supported catalysts for the total oxidation of VOCs: adjusting structure and acidity of MWW zeolite support. (2020) (in preparation)
2. **Zhou, Y.**, Kadam, S.A., Shamzhy, M., Čejka, J., Opanasenko, M., Isoreticular UTL-derived zeolites as model materials for probing pore size–activity relationship. 2019, *ACS Catalysis*, 9(6), 5136-5146.
3. **Zhou, Y.**, Žilková, N., Shamzhy, M., Avadhut, Y., Hartmann, M., Čejka, J., Opanasenko, M., Novel approach towards Al-rich AFI for catalytic application. 2019, *Applied Catalysis A: General*, 577, 62-68.

4. Chen, H., **Zhou, Y.**, Tošner, Z., Čejka, J., Opanasenko, M., Synthesis of aggregation-resistant MFI nanoparticles. 2019, *Catalysis Today*. (10.1016/j.cattod.2019.10.026)
5. **Zhou, Y.**, Huang, Y., Li, L., Gong, Y., Liu, X., Zhang, X., Sun, C.Q., Hydrogen-bond transition from the vibration mode of ordinary water to the (H, Na) I hydration states: Molecular interactions and solution viscosity, 2018, *Vibrational Spectroscopy*, *94*, 31-36.
6. **Zhou, Y.**, Zhong, Y., Liu, X., Huang, Y., Zhang, X., Sun, C.Q., NaX solvation bonding dynamics: hydrogen bond and surface stress transition (X= HSO₄, NO₃, ClO₄, SCN), 2017, *Journal of Molecular Liquids*, *248*, 432-438.
7. Zhang, X., **Zhou, Y.**, Gong, Y., Huang, Y., Sun, C., Resolving H (Cl, Br, I) capabilities of transforming solution hydrogen-bond and surface-stress, 2017, *Chemical Physics Letters*, *678*, 233-240.
8. Zhang, X., Xu, Y., **Zhou, Y.**, Gong, Y., Huang, Y., Sun, C.Q., HCl, KCl and KOH solvation resolved solute-solvent interactions and solution surface stress, 2017, *Applied Surface Science*, *422*, 475-481.
9. Gong, Y., Xu, Y., **Zhou, Y.**, Li, C., Liu, X., Niu, L., Huang, Y., Zhang, X., Sun, C.Q., Hydrogen bond network relaxation resolved by alcohol hydration (methanol, ethanol, and glycerol), 2017, *Journal of Raman Spectroscopy*, *48*(3), 393-398.
10. **Zhou, Y.**, Gong, Y., Huang, Y., Ma, Z., Zhang, X., Sun, C.Q., Fraction and stiffness transition from the HO vibrational mode of ordinary water to the HI, NaI, and NaOH hydration states, 2017, *Journal of Molecular Liquids*, *244*, 415-421.
11. **Zhou, Y.**, Wu, D., Gong, Y., Ma, Z., Huang, Y., Zhang, X., Sun, C.Q., Base-hydration-resolved hydrogen-bond networking dynamics: Quantum point compression, 2016, *Journal of Molecular Liquids*, *223*, 1277-1283.
12. Gong, Y., **Zhou, Y.**, Wu, H., Wu, D., Huang, Y., Sun, C.Q., Raman spectroscopy of alkali halide hydration: hydrogen bond relaxation and polarization, 2016, *Journal of Raman Spectroscopy*, *47*(11), 1351-1359.
13. **Zhou, Y.**, Huang, Y., Ma, Z., Gong, Y., Zhang, X., Sun, Y., Sun, C.Q., Water molecular structure-order in the NaX hydration shells (X= F, Cl, Br, I), 2016, *Journal of Molecular Liquids*, *221*, 788-797.
14. **Zhou, Y.**, Zhong, Y., Gong, Y., Zhang, X., Ma, Z., Huang, Y., Sun, C.Q., Unprecedented thermal stability of water supersolid skin, 2016, *Journal of Molecular Liquids*, *220*, 865-869.
15. Zeng, Q., Yan, T., Wang, K., Gong, Y., **Zhou, Y.**, Huang, Y., Sun, C.Q., Zou, B., Compression icing of room-temperature NaX solutions (X= F, Cl, Br, I), 2016, *Physical Chemistry Chemical Physics*, *18*(20), 14046-14054.
16. 宫银燕, **周勇**, 黄勇力, 孙长庆, 受激氢键(O:H-O)分段长度和能量的声子计量谱学测定方法, CN Patent CN 105403515 A, 2018.

Conferences: oral and poster presentations

1. **Workshop on Layered Materials**, oral presentation, “Isorecticular UTL-derived zeolites as model materials for probing pore size-activity relationship”, 2-6 September, 2019, Liblice, Czech Republic.
2. **FCCat 2019-French Conference on Catalysis 2019**, poster presentation, “Novel approach towards Al-rich AFI for catalytic application”, 3-7 June, 2019, Fréjus, France.
3. **School of catalysis**, oral presentation, “Novel approach towards Al-rich AFI for catalytic application”, 13-15 May, 2019, Liblice, Czech Republic
4. **50th Symposium on Catalysis**, oral presentation, “Isorecticular zeolites as model materials for probing pore

- size-activity relationship”, 5-6 November, 2018, Prague, Czech Republic.
5. **7th International Workshop on Layered Materials**, poster presentation, “Synthesis of carbon with two-dimensional zeolites as templates”, 9-13 September 2018, Kraków, Poland.
 6. **19th International Symposium on the Reactivity of Solids (ISRS-19)**, poster presentation, “Luminescent and catalytic properties modulation of germanosilicate zeolite AFI by post-synthesis alumination”, 15-18 July, 2018, Bayreuth, Germany.
 7. **EFCATS School on Catalysis**, poster presentation, “Isomorphously incorporation of aluminum into isoreticular zeolites: pore size effect on catalyst activity”. 25-29 June, 2018, Liblice, Czech Republic.
 8. **Advances in Zeolite Chemistry and Catalysis**, oral presentation, “Isomorphously incorporation of aluminum into isoreticular zeolites: pore size effect on catalyst activity”. 21-25 May, 2018, Český Krumlov, Czech Republic.
 9. **Workshop on Layered Materials**, oral presentation, “Tetrahydropyranylation of alcohols on isomorphously substituted isoreticular zeolites”, 1-5 September, 2017, Třešt, Czech Republic.
 10. **Seminar of Students 2017**, oral presentation, “Substituted isoreticular zeolites with UTL topology”, 9-10 May, 2017, Liblice, Czech Republic.